UvA-DARE (Digital Academic Repository)

XMM-Newton X-ray study of early type stars in the Carina OB1 association

Antokhin, I.I.; Rauw, G.; Vreux, J.M.; van der Hucht, K.A.; Brown, J.C.

Link to publication

Astronomy
&
Astrophysics

XMM-Newton X-ray study of early type stars
in the Carina OB1 association[*],[**]

I. I. Antokhin[1,2,3], G. Rauw[2,***], J.-M. Vreux[2], K. A. van der Hucht[4,5], and J. C. Brown[3]

[1] Sternberg Astronomical Institute, Moscow University, Universitetskij Prospect 13, Moscow 119992, Russia
    e-mail: igor@sai.msu.ru
[2] Institut d'Astrophysique et de Géophysique, Université de Liège, Allée du 6 août, 17 Bât. B5c, 4000 Liège, Belgium
[3] Department of Physics and Astronomy, University of Glasgow, Kelvin Building, Glasgow G12 8QQ, Scotland, UK
[4] SRON Netherlands Institute for Space Research, Sorbonnelaan 2, 3584 CA Utrecht, The Netherlands
[5] Astronomical Institute Anton Pannekoek, University of Amsterdam, Kruislaan 403, 1098 SJ Amsterdam, The Netherlands

ABSTRACT

Aims. X-ray properties of the stellar population in the Carina OB1 association are examined with special emphasis on early-type stars. Their spectral characteristics provide some clues to understanding the nature of X-ray formation mechanisms in the winds of single and binary early-type stars.
Methods. A timing and spectral analysis of five observations with XMM-Newton is performed using various statistical tests and thermal spectral models.
Results. 235 point sources have been detected within the field of view. Several of these sources are probably pre-main sequence stars with characteristic short-term variability. Seven sources are possible background AGNs. Spectral analysis of twenty four sources of type OB and WR 25 was performed. We derived spectral parameters of the sources and their fluxes in three energy bands. Estimating the interstellar absorption for every source and the distance to the nebula, we derived X-ray luminosities of these stars and compared them to their bolometric luminosities. We discuss possible reasons for the fact that, on average, the observed X-ray properties of binary and single early type stars are not very different, and give several possible explanations.

Key words. stars: early-type – stars: binaries: general – X-rays: stars

1. Introduction

Although X-ray emission by early-type stars is nowadays well established, its origin is still not fully understood. Observations with the *Einstein*, *ROSAT* and *ASCA* satellites indicated that hot luminous stars have rather soft thermal X-ray spectra. This picture contrasts with the expected spectral properties if the X-rays were produced in a hot corona at the base of the stellar wind (e.g. Waldron 1984). Indeed, in the latter case one would expect to observe substantial absorption of the softest emission. The lack of this absorption in the observed spectra triggered the elaboration of an alternative scenario. In fact, according to the phenomenological model proposed by Lucy & White (1980) and further elaborated by Lucy (1982), hydrodynamic shocks are generated throughout a radiation-driven stellar wind as the consequence of the intrinsic instabilities of radiative driving. The velocity jumps in such shocks heat the post-shock plasma to temperatures of a few million degrees. These shocks would be distributed throughout the stellar wind with the result that even soft X-rays could escape the wind without substantial absorption. Recent theoretical studies of such instabilities have been presented for instance by Feldmeier et al. (1997), Owocki & Cohen (1999), and Dessart & Owocki (2002). High resolution spectra obtained with the new generation of X-ray observatories have confirmed the thermal origin of the bulk of the X-ray emission from early-type stars (e.g. Kahn et al. 2001), but in some cases, the properties of the observed line profiles led also to new challenges for the shock model (see e.g. Rauw 2006, for a review).

Another well established, though yet unexplained, property of the X-ray emission of hot stars is the linear scaling between the observed X-ray luminosity (L_X) and the bolometric luminosity (L_{bol}). Using *Einstein* data, Long & White (1980), Pallavicini et al. (1981) and Chlebowski et al. (1989) found that $L_X \simeq 10^{-7} \times L_{bol}$ for OB stars. *ROSAT* observations broadly confirmed this relation. Berghöfer et al. (1997) and Kudritzki et al. (1996) found that including a weak dependence on the characteristic wind density leads to a somewhat tighter relationship. However, considering the scaling of the X-ray emission with various wind and stellar properties in the framework of the shock model, Owocki & Cohen (1999) found that a delicate equilibrium between emission and absorption is required to reproduce the empirically derived $L_X - L_{bol}$ relation. With the broader energy range and improved sensitivity of the new generation of

X-ray satellites it is important to re-address the question of the empirical $L_X - L_{bol}$ scaling for OB stars.

When doing this it is crucial to pay attention to the multiplicity of the stars in the sample. Indeed, in OB binaries, the collision of the two stellar winds is expected to generate a strong X-ray bright shock between the stars (see e.g. Stevens et al. 1992) and this feature is believed to manifest itself as an "excess" in the L_X/L_{bol} ratio (see e.g. Pollock 1995). Moreover, since the relative velocities of colliding winds can be much higher than the shock velocity jumps in winds of single stars, the X-ray spectra of colliding wind early type binaries can be quite hard. In fact the hardness of the observed spectra of some early-type stars, and, in particular, the presence of the Fe XXV and Fe XXVI lines at 6.7 keV indicative of very hot material has been suggested as an indication of possible binarity (e.g. Raassen et al. 2003).

This latter suggestion leads to an interesting question. Clearly in a general case it is very difficult to "hide" such a hard secondary component of a colliding wind binary. Indeed, to produce strong hard X-ray emission, the companion must be a massive hot star, and as such, should manifest itself in other wavelength domains (e.g. optical spectra) and also via orbital spectral and photometric variability in the X-rays. Traditionally, a lack of variations was attributed to a "pole-on" orientation of the binary orbit. However, lately, a growing number of examples of apparently single O and WR stars with hard X-ray spectra (e.g. Skinner et al. 2002; Raassen et al. 2003, the present study) has become available. It seems unlikely that all these objects are binaries seen from their orbital poles. Thus the question is whether there exists another, yet unknown, mechanism which could produce hard X-rays in single star winds? Exceptions to this rule are stars such as θ^1 Ori C with strong enough magnetic fields to confine the stellar wind into the plane near the magnetic equator (Cassinelli et al. 2003; Brown et al. 2003; Maheswaran 2003; Gagné et al. 2005; Li et al. 2007). In such cases, the head-on collision of the winds from the two hemispheres of a single star produces a rather hard X-ray emission. The fundamental problem here is that the only source of energy in the classical picture of a hot star wind which is able to produce high temperatures and hence hard thermal X-rays, is the wind kinetic energy. But to release most of this energy through radiation one needs a "wall" able to stop the supersonic flow and heat the material in the formed shock. In the winds of single stars we do not expect to find such a wall except in the magnetised case. On the other hand, there is a number of known early-type binaries which show neither significant X-ray excess nor particularly hard X-ray spectra. What could be the mechanism which dumps the X-ray production in these systems?

The Carina OB 1 association with its impressive number of early-type stars – including some of the youngest, hottest and most massive objects known in our Galaxy – is an ideal place to investigate the X-ray properties of these objects. The history of X-ray studies of the region goes back to the *Einstein* era. Seward et al. (1979) presented *Einstein* X-ray (0.2−4.0 keV) observations of the Carina open cluster Tr 16 and its environment, including six O-type stars and one WR star, WR 25. Subsequent *Einstein* observations by Seward & Chlebowski (1982) of the same region showed X-rays from 15 O-type and WR stars. More studies were performed with the use of the *ROSAT* and *ASCA* satellites. Some of them were focused on individual objects like the LBV η Car (Corcoran et al. 2000, and references therein) or WR 25 (e.g. Pollock & Corcoran 2006; Skinner et al. 1995). Others were devoted to investigating general X-ray properties of the early-type stars population (Corcoran 1999, and references therein).

Recently, four studies of the region based on X-ray observations with *Chandra* and *XMM-Newton* satellites were published. Evans et al. (2003) (hereafter EV03) and Evans et al. (2004) (hereafter EV04) using *Chandra* data, detected 154 point sources, 23 of which are of O, B types. They present luminosities and hardness ratios for the detected sources and confirm the $L_X - L_{bol}$ relation for early-type stars. They also discuss the low-resolution spectra of the 14 brightest sources. Sanchawala et al. (2007), using the same *Chandra* data as EV03 plus another archival *Chandra* data set, detected 454 sources in the region, among which 38 are known OB stars. The latter paper is focused on cross-identification of the X-ray sources with optical and near-infrared imaging observations specifically obtained for this study. This allowed the authors to conclude that about 300 sources are likely late-type pre-main-sequence stars. The X-ray luminosities of the detected OB stars were estimated based on their count rate and using a single-temperature Raymond-Smith model of thermal plasma with $\log T = 6.65$ (0.384 keV). Albacete-Colombo et al. (2003) (hereafter AC03) detected 80 discrete sources in the region using two observations by *XMM-Newton* (revolution numbers 115 and 116). They discuss X-ray properties of the sources, including the $L_X - L_{bol}$ relation for early-type stars. In the present paper, we used three additional *XMM-Newton* observations, which allow us to increase the signal to noise ratio and to detect more than 200 discrete sources. We shall compare our results with those of AC03 throughout the current paper. We do not present a detailed spectral analysis of individual objects in this paper as many such objects deserve dedicated papers. A detailed study of WR 25 based on the same *XMM-Newton* data as in the current study was published by Raassen et al. (2003), whilst η Car has been the subject of many studies including those utilizing extensive data sets obtained with various X-ray observatories (see, e.g., Leutenegger et al. 2003; Weis et al. 2004; Viotti et al. 2004; Corcoran 2005; Hamaguchi et al. 2007). Analysis of other interesting objects (e.g. the early type binary HD 93205) will be the subject of forthcoming papers.

The goals of this paper are:

– to describe general X-ray properties of the detected sources;
– to look for their variability, both short and long term;
– to investigate the L_X/L_{bol} relation for early type stars;
– to compare X-ray properties of single versus binary early-type stars and to try to get some clues to their differences and similarities.

The structure of the paper follows these outlined priorities. In the second section, the observational details are given. Source detection, their identification with the optical and IR catalogues, X-ray count rates, identification of possible extragalactic sources are given in Sect. 3. Section 4 provides general information about open clusters in the Carina nebula, along with the discussion of their distance from the Earth. The results of the variability study are presented in Sect. 5. The X-ray properties of early-type stars detected in the region are presented in Sect. 6. We discuss our results in Sect. 7 and a short summary is given in Sect. 8.

2. Observations

The observations of the Carina region were obtained with the Reflection Grating Spectrometers (RGS) and the European Photon Imaging Camera (EPIC) CCD detectors of the *XMM-Newton* observatory. The log of EPIC observations is shown in Table 1.
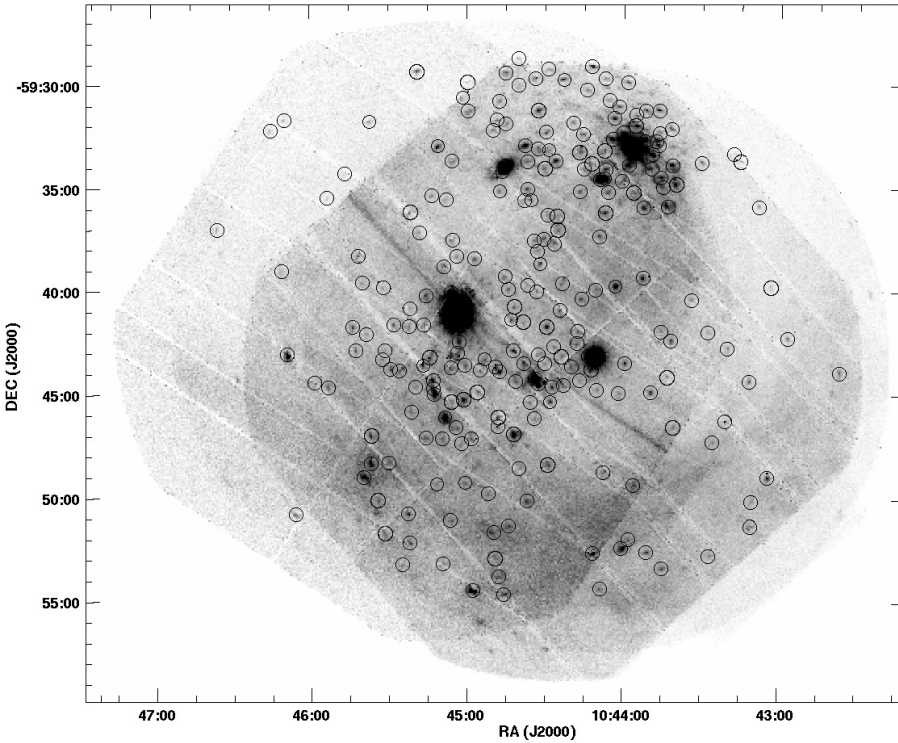
Fig. 1. Mozaiced exposure-corrected image of the field, combining all data sets and all instruments MOS1, MOS2, and PN. Energy range 0.4−10.0 keV. Positions of the detected sources are shown.

Table 1. Log of the Carina region observations by *XMM-Newton*.

Data set number	1	2	3	4	5
revolution	#115	#116	#283	#284	#285
Obs. date	26-7-2000	27-7-2000	25-6-2001	28-6-2001	30-6-2001
Start (UT)	04:58	23:48	06:51	07:22	04:38
Instrument	Integration Time				
	(h)				
MOS 1	9.4	3.1	10.2	11.7	10.4
MOS 2	8.5	2.3	10.2	11.7	10.4
PN	8.8	2.6	9.6	11.0	9.7

In the two first data sets the primary target was η Car while in the third to fifth data sets the primary target was WR 25. The analysis of RGS and EPIC observations of WR 25 was presented in Raassen et al. (2003) while the RGS analysis of η Car was published by Leutenegger et al. (2003) and we will not repeat these here. In Fig. 1 we show the mozaiced image of the area combined from all 5 data sets and 3 EPIC instruments.

The EPIC-MOS and PN instruments were operated in the full frame mode except during rev. 115 and 116 where MOS2 was operated in the small window mode. All three EPIC instruments used the thick filter to reject optical light. We used version 7.0 of the *XMM-Newton* Science Analysis System (SAS) software to reduce the raw EPIC data. For spectral analyses, we adopted the most up-to-date redistribution matrices provided by the EPIC instrument teams and used SAS to build the appropriate ancillary response file for each observation. More details on the pipeline processing of the data are given in Raassen et al. (2003).

3. Source detection and cross-identification

3.1. Source detection

Sources were detected and count rates measured in three energy bands – soft (0.4−1.0 keV), medium (1.0−2.5 keV), and hard (2.5−10.0 keV). The choice of these bands is based on the following considerations:

- there is a lot of noise (sometimes systematic features) in the PN data for $E < 0.4$ keV;
- the EPIC sensitivity above 10 keV is almost zero;
- the relatively narrow soft band is sensitive to interstellar absorption;
- the wide hard band allows one to collect more photons and hence improve statistics.

Source detection and determination of source parameters was performed with the SAS `edetect_chain` metatask based on the *sliding cell detection* and *maximum likelihood* (ML) methods. The ML method (the SAS task `emldetect`) makes use of maximum likelihood PSF (point spread function) fitting to the source count distribution. The so-called logarithmic detection likelihoods obey the simple relationship $L_2 = -\ln(p)$ where p is the probability for a random Poissonian fluctuation to have caused the observed source counts. The threshold for inclusion of sources in the final output was set to $L_2^{min} = 10.0$. In the limit of a very large number of counts, the likelihood function is a Gaussian and the logarithmic likelihood becomes a parabola. At this limit the value of 10.0 is equivalent to 3 sigmas.

To increase the signal-to-noise ratio and thus to detect as many sources as possible, we merged the event lists and images from different data sets. Unfortunately, the angular distance between the central axes of the data sets 1 and 2 on one hand, and 3 to 5 on the other, is too large (~7′) and does not allow one to merge all data sets into a single coordinate system without producing spurious results in the subsequent source detection. For this reason we merged the data sets 1 and 2, and the data sets 3, 4, 5 separately. The source detection was performed on the two resulting merged sets of data, making use of all energy bands and all instruments simultaneously. The resulting source lists were visually inspected and a few spurious detections, mainly along the CCD edges, were removed.

The coordinates of the sources common in the two merged data sets are very close and do not show any systematic differences. We attempted to use the `eposcorr` procedure to improve the coordinates by cross-correlating the XMM coordinates with the Two Micron All Sky Survey point source catalogue[1] (2MASS, Skrutskie et al. 1997) and the optical sources in the SIMBAD database. In both cases, neither a significant systematic shift nor a field rotation was apparent. The corrections in RA and Dec were less than 0.5″ and not consistent between the IR and optical catalogues. We conclude that the procedure does not allow one to improve the *XMM-Newton* coordinates. For the final source list the coordinates of the sources common in the two merged data sets were averaged. As some of the detected sources may be variable, it is of interest to measure their count rates not just in the merged data sets but in every individual one. For this purpose, we repeated the ML routine with our source list as the input, for the data sets 1−5.

The total number of detected sources is 235. Recall that AC03, using the data sets 1 and 2, detected 80 sources. Sanchawala et al. (2007) were able to detect 454 sources in the *Chandra* data on the field, thanks to the superior angular resolution of the *Chandra* telescope. Figure 1 shows the positions of the detected sources over the mozaiced image of the field. A sample of the catalogue of the detected discrete X-ray sources is presented in Table 2. The full table is available as online data. The table includes only those measurements in which the total logarithmic EPIC likelihood exceeds the value of 10.0.

One should note that the count rates in Table 2 may be systematically different from those provided for the same stars by AC03. One evident reason is that we used different energy limits for our soft, medium, and hard bands than AC03. A deeper reason, is, however, that AC03 used the wavelet technique (the SAS `ewavelet` routine) to estimate their count rates. Using `ewavelet` is equivalent to fit a Gaussian to the observed discrete source image. However, the actual EPIC PSF is quite different from a Gaussian. The `emldetect` routine makes use of an empirical PSF and thus, according to the SAS manual, should provide more accurate count rate estimates than `ewavelet`. Our tests show that the AC03 count rates are systematically lower than the count rates obtained for the same energy band with `emldetect`.

Fluxes and luminosities can be calculated from count rates provided that the response function of the telescope is known and certain assumptions are made about the emission model, interstellar absorption and distance to the region. We used `xspec` to calculate the conversion factors. A combination of models `wabs*apec` was used. Here `apec` is an emission spectrum from a hot optically thin thermal plasma. The APEC code (Smith et al. 2001) is a modern version of the well-known model of Raymond & Smith (1977). `wabs` is an interstellar medium (ISM) absorption model. As we are most interested in X-ray properties of hot massive stars, the plasma temperature in the `apec` model was set to $kT = 0.6$ keV, a value typical for X-ray emission produced by shocks formed in stellar winds of early-type stars. The interstellar absorption over the field is relatively uniform with $E(B-V) = 0.52$ mag (Massey & Johnson 1993). Using a well-known transformation from Bohlin et al. (1978) $N_H = 5.8 \times 10^{21} \times E(B-V)$ this translates to a column density $N_H = 3 \times 10^{21}$ cm^{-2}. We used this value in the `wabs` model. Using the above combination of models and *XMM-Newton* response

function we derive the conversion factors for MOS and PN instruments in the 0.4−10.0 keV energy range as

$$F_{a,MOS} = 0.76 \times 10^{-11} \, \text{erg cm}^{-2} \, \text{s}^{-1} \times \text{cr}$$

$$F_{a,PN} = 0.23 \times 10^{-11} \, \text{erg cm}^{-2} \, \text{s}^{-1} \times \text{cr}$$

$$F_{0,MOS} = 2.01 \times 10^{-11} \, \text{erg cm}^{-2} \, \text{s}^{-1} \times \text{cr}$$

$$F_{0,PN} = 0.61 \times 10^{-11} \, \text{erg cm}^{-2} \, \text{s}^{-1} \times \text{cr}$$

where cr is the corresponding count rate, the indices "a" and "0" mark the absorbed and unabsorbed fluxes respectively. Luminosities can be readily obtained from the above fluxes assuming a distance to the nebula of 2.5 kpc (see Sect. 6). We caution that the conversion from count rates to energy is very model-dependent and can only be used as a very rough estimation of the flux. Below we provide individual fluxes for the brightest sources which allow spectral fitting.

3.2. The detection limit

Evaluation of the detection limit of our observations is not a trivial task. First, this limit is a priori not uniform throughout the field of view as the *XMM-Newton* effective exposure duration is decreasing from the center of the FOV towards the edges. Second, as different sources in our catalogue were detected in different observations or their combinations, the detection limits in the intermediate partial source lists are different.
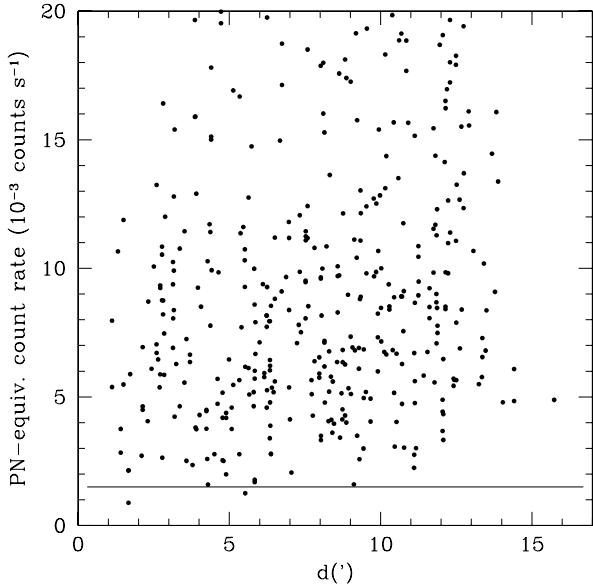
Thus, to estimate the overall limit, we adopted a completely empirical approach, taking advantage of the large number of X-ray sources in the field. We assumed that a good indication of the detection limit in the different parts of the field is given by the brightness of the faintest sources detected in these areas. Due to the presence of gaps, not all sources which are detected in the MOS images, are also present in the PN ones. To increase statistics, we first computed an equivalent PN count rate, in the range 0.4−10.0 keV, for each source missing in the PN images. To first order, the relation between the count rates measured in any of the two MOS detectors and in the PN detector is linear. We found the conversion factor using the count rates of the sources, which were detected in all three EPIC instruments. Figure 2 displays the source PN-equivalent count rates as a function of the distance from the central axis of the FOV. A lower limit is clearly seen in the distribution. Towards the edges of the FOV, the limit is increased as expected. The faintest sources in the region have the PN-equivalent count rate about 1.5×10^{-3} counts s^{-1}, which we accept as our detection limit. In terms of flux, using the conversion above, this limit amounts to 3.3×10^{-15} erg cm^{-2} s^{-1}.

3.3. Cross-identification

We have cross-correlated the positions of the 235 sources with various optical and infrared catalogues. The 2MASS catalogue provides the most complete coverage of the Carina complex. We therefore selected this catalogue to determine the optimal radius of cross-correlation. To this aim, we adopted the approach outlined by Jeffries et al. (1997) and applied to the *XMM-Newton* data of the young open clusters NGC 6530 and NGC 6383 by Rauw et al. (2002, 2003). The distribution of the cumulative number of catalogued sources as a function of the cross-correlation radius r is given by

$$\Phi(d \leq r) = A \left[1 - \exp\left(\frac{-r^2}{2\sigma^2} \right) \right]$$
$$+ (N - A) \left[1 - \exp\left(-\pi \, B \, r^2 \right) \right]$$

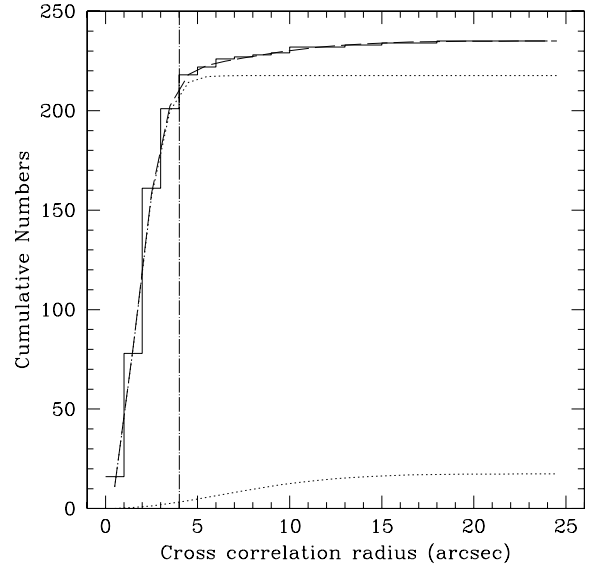[1] See `http://irsa.ipac.caltech.edu/`.

Fig. 2. Bottom part of the distribution of the PN-equivalent count rates of the X-ray sources as a function of their distance d to the center of the FOV. The horizontal line shows the adopted detection limit.

Fig. 3. Cumulative numbers of correlations between the X-ray detections and the 2MASS catalogue objects as a function of the correlation radius. The dotted curves correspond to the best fitting expressions for the real and spurious correlations. The dashed curve yields the sum of these terms and the dash-dotted vertical line corresponds to the adopted correlation radius of 4.0″.

where N, A, σ and B stand respectively for the total number of cross-correlated X-ray sources ($N = 235$), the number of true correlations, the uncertainty on the X-ray source position and the surface density of catalogue sources. For further details on the method we refer to the work of Jeffries et al. (1997). The fitting parameters A, σ and B were obtained from the best fit to the actual distribution displayed in Fig. 3. For the 2MASS catalogue, we derive $A = 217.6$, $\sigma = 1.6″$ and $B = 0.004$ arcsec^{-2}. The optimal radius that includes the majority of the true correlations while simultaneously limiting contamination by spurious correlations, is found to be around 4.0″. We thus consider an infrared source as a possible counterpart if it falls within 4.0″ of the coordinates of the X-ray source. This is significantly smaller than the corresponding optimal radius for the *XMM* data on NGC 6383. The main reason is the larger surface density of 2MASS sources in the Carina region. For $r = 4.0″$, we expect statistically to achieve 208 true and 6 spurious correlations.

We have also cross-correlated the positions of our X-ray sources with the AC03 *XMM-Newton* and EV03 *Chandra* X-ray surveys of the field, using a similar technique. The optimal cross-correlation radii were found to be around 5.0″ for the AC03 and 4.5″ for the EV03 data statistically providing around 58/3 and 54/5 true/false correlations respectively.

The results of the correlations with the 2MASS and X-ray catalogues and the results of various optical studies of the Carina Nebula are listed in Table 3. The source designation in this table follows the naming conventions recommended by the IAU for serendipitous sources detected with *XMM-Newton*: the XMMU J prefix is followed by the right ascension HHMMSS.s (in hours, minutes, seconds and tenths of seconds, equinox J2000) and the declination of the source +/−DDMMSS (in degrees, arcminutes and arcseconds, equinox J2000), both truncated not rounded. The designations of the sources identified with the AC03 catalogue are taken from that catalogue; note that we still provide our own coordinates of such sources. 167 EPIC sources have a single 2MASS optical counterpart within a radius of less than 4.0″. The average angular separation between the X-ray source and the optical counterpart is $(2.3 \pm 0.9)″$. Cudworth et al. (1993) performed

a proper motion study of the open clusters in the Carina complex. Using photographic plates spanning about a century, they derived membership probabilities for 577 stars. We have cross-correlated the astrometry of our EPIC sources with the catalogue of Cudworth et al. Information on proper motion membership probabilities is provided in the last column of Table 3.

Finally, given the limiting sensitivity of 1.5×10^{-3} counts s^{-1} for PN and the size of the field of view (roughly 0.25 square degree), we can use the $\log N - \log S$ relation of Motch et al. (2003) for $b \sim 0°$ to estimate the number of field stellar sources. In this way, we find that about 50−70 field stars could be detected. Since the Motch et al. (2003) relation was established from fields that do not harbour star formation regions, the significantly larger number of sources detected in our Carina field clearly results from X-ray sources associated with the clusters in the field of view.

3.4. Extragalactic background sources

The line of sight towards η Car ($l_{\mathrm{II}} = 287.60°$, $b_{\mathrm{II}} = -0.63°$) is nearly tangent to the Carina spiral arm. As a result, the neutral hydrogen column density along this direction must be quite large and should produce a substantial absorption of X-ray photons from extragalactic background sources (EBS).

To get a rough first order estimate of the total Galactic extinction along this line of sight, we made use of the *DIRBE/IRAS* extinction maps provided by Schlegel et al. (1998). Schlegel et al. caution that one has to be careful when using these maps near the Galactic plane. Moreover, the interstellar extinction in the Carina region is rather patchy and its properties could deviate from those of the average Galactic extinction curve (e.g. Carraro et al. 2004). With these limitations in mind, we find that the *DIRBE/IRAS* maps indicate a rather large, but highly variable $E(B - V)$ colour excess (between ~6.4 on average at the edges of the EPIC field and ~14.5 near η Car). Converting these values into neutral hydrogen column densities by means of the gas to

dust ratio of Bohlin et al. (1978), we estimate N_H in the range 3.7–8.5×10^{22} cm^{-2}.

Assuming that EBSs (most of which are probably Active Galactic Nuclei (AGN)) have a power-law spectrum with a photon index of 1.4 (Giacconi et al. 2001), and suffer a total interstellar absorption of 3.7–8.5×10^{22} cm^{-2}, the above detection limits translate into unabsorbed fluxes of 1.0–1.5×10^{-14} erg cm^{-2} s^{-1} and 2.8–4.3×10^{-14} erg cm^{-2} s^{-1} in the 0.5–2.0 keV and 2.0–10 keV band respectively. From the $\log N - \log S$ relation of Giacconi et al. (2001), we expect to detect between ∼16 and 24 extragalactic background sources.

To discriminate these sources from the Galactic ones, the following basic properties of AGNs could in principle be used (see e.g. Fiore 1997; Nandra 2001; Bauer et al. 2004):

1. the spectra of AGNs are power laws with the canonical intrinsic X-ray spectral slope $\Gamma \sim 1.9$–2.0. The average observed spectral slope of EBS is about 1.4 (Giacconi et al. 2001);
2. their flux is variable on timescales from a few hours to years.

In practice, it is impossible to fit the individual source spectra since the candidates are very faint and the count statistics poor. For this reason, we have simulated the values of two PN hardness ratios $HR_1 = (M - S)/(M + S)$ and $HR_2 = (H - M)/(H + M)$ for a grid of simple models. Within `xspec`, we have used the PN response matrices to generate fake spectra corresponding to differently absorbed power law spectra. We considered three photon indices $\Gamma = 1.4, 1.7, 2.0$ and several neutral hydrogen densities $N_H = (0.1, 0.3, 1.0, 3.0, 7.0, 11.0, 15.0) \times 10^{22}$ cm^{-2}. We then compared these simulated hardness ratios with the observed ones of all discrete sources not identified with optical or infra-red catalogues. For the list of the potential EBS candidates, we select those sources whose errorboxes cover the simulated hardness ratios. The resulting EBS candidates are the sources 3, 6, 119, 124, 170, 185, 207. Their total number is seven which is lower than the estimation above; still the estimation gives only a rough idea about the number of the background sources, given the uncertainties involved.

4. Open clusters in the Carina nebula

The region covered by our EPIC data harbours several young open clusters that are extremely rich in hot massive stars; the most important ones being Trumpler 14 and 16. Tr 14 is a compact cluster containing three very hot O3 stars. Tr 14 is probably emerging from the eastern and near side of the dense parental molecular cloud (Tapia et al. 2003). Tr 14 might be slightly younger than Tr 16 as suggested by a fainter absolute magnitude and a larger He II λ 4686/ He II λ 4541 ratio in the spectra of early and mid O-type dwarfs (Walborn 1995). Collinder 232 is probably not a physical entity but a condensation of stars in the vicinity of Tr 14 and 16 (see e.g. Walborn 1995; Tapia et al. 2003). In a similar way, Collinder 228 could actually be part of Tr 16. The apparent distinction between the two clusters might result from obscuration by a dust lane (Walborn 1995). Note an alternative view of Carraro et al. (2004) who argue that Collinder 232 may be a physical aggregate (a rather sparse young open cluster), based on the comparison of its colour-magnitude diagrams and theoretical zero age main sequence (ZAMS) tracks.

The extinction in the Carina complex has been subject to much controversy. Conflicting conclusions ranging from a normal uniformly high to an anomalous and variable extinction have been proposed. This dilemma has important consequences for a consistent determination of the distance moduli (see e.g. the discussion in Walborn 1995). In addition, since the line of sight is along the direction of a galactic spiral arm, there are probably many foreground and background objects that appear projected onto the Carina Nebula.

The exact ages of the clusters and the star formation history of the Carina Nebula are other tricky issues. Up until recent years, evidence for ongoing star formation in the Carina Nebula was rather scarce. Megeath et al. (1996) and Rathborne et al. (2002) reported evidence of star formation triggered in the molecular cloud exposed to the ionizing radiation of the hot stars of the Carina Nebula. None of the three near-IR sources N 1, N 3 and N 4 proposed to be associated with embedded recently born O-stars is detected in our X-ray data. More recently, Smith et al. (2003) reported the discovery of dozens of candidates of so-called proplyds in the Carina Nebula, clearly demonstrating that the formation of low and intermediate mass stars is actively proceeding. We note that none of the objects discussed by Smith et al. (2003) is detected as an X-ray source in our EPIC data.

DeGioia-Eastwood et al. (2001) obtained *UBV* photometry of the Carina clusters. They found a significant population of pre-main sequence stars in Tr 14 and Tr 16 that have been forming over the last 10 Myr whilst the most massive stars in Tr 16 have ages between 1 and 3 Myr (with one exception, a star in the 5–6 Myr range in each cluster). According to their results, intermediate mass star formation seem to have proceeded continuously over the past 10 Myr and the formation of intermediate mass stars started well before that of OB stars and was apparently not disrupted by the formation of these OB stars. Finally, Tapia et al. (2003) performed an extended *UBVRIJHK* photometric study of the clusters in the Carina Nebula. They infer ages between less than 1 Myr and 6 Myr for Tr 14 and 16. A small number of IR excess stars were found in both clusters. Tapia et al. further detected a population of 19 near-IR sources in the Car I HII region whose formation could have been triggered by the action of the early-type stars. We note that none of these objects is detected in our EPIC data.

Corcoran (1999) analysed ROSAT-HRI observations of the Carina complex. While he found the L_X/L_{bol} ratio of early-type stars to spread between 10^{-8} and 10^{-6}, he did not find evidence for a population of X-ray bright pre-main sequence (PMS) stars. However, he cautioned that the failure to detect these objects could simply be due to the limited sensitivity of the ROSAT satellite.

Trumpler 16 is particularly rich in massive binaries (see e.g. Levato et al. 1991). The properties of several eclipsing or ellipsoidal early-type binaries (HD 93205, Morrell et al. 2001; Antokhina et al. 2000; Tr 16-1, Freyhammer et al. 2001; and Tr 16-104, Rauw et al. 2001) have been investigated recently. The components of the three binaries are all found to lie pretty close to the zero-age main sequence suggesting that they may be younger than 1 Myr (Rauw 2004). The absolute magnitudes determined from the study of these eclipsing binaries suggest a distance modulus (DM) of 11.95 ± 0.06 (corresponding to a distance of 2.45 kpc) lower than the value of DM = 12.55 ± 0.1 (which corresponds to a distance of 3.24 kpc) derived by Massey & Johnson (1993) and Massey et al. (2001) from a spectroscopic and photometric study of the Trumpler 14 and 16 clusters. Allen & Hillier (1993), Meaburn (1999), and Davidson et al. (2001) investigated the geometry and kinematics of the Homunculus Nebula and found the distance to η Car around $2.3 \pm \sim 0.3$ kpc. Tapia et al. (2003) derived the average distance to Tr 14, Tr 15 and Tr 16 to be $d = 2.7$ kpc from their *UBVRIJHK* photometric study, although they note a very large scatter in d.

Carraro et al. (2004) confirm the distance of 2.5 kpc to Tr 14 but reach a different conclusion about the distance to Tr 16. Comparing the colour-magnitude diagrams and the Hertzsprung-Russel diagram (based on their *UBVRI* photometry) with post and pre-main sequence tracks and isochrones, they find that Tr 16 lies at the distance of about 4 kpc from the Sun. EV03 adopted the distance of 2.5 kpc to the clusters in the Carina Nebula. In the current study we also adopt the distance of 2.5 kpc to all stars in the region. Note that while the absolute value of the X-ray and bolometric luminosities will change with the distance, their ratio remains unchanged.

Figure 4 illustrates the JHK_s colour−colour diagram of the 2MASS infrared counterparts identified in our current study. We have included only those objects that were detected in all three filters J (1.25 μm), H (1.65 μm) and K_s (2.17 μm) with a photometric accuracy better than $\sigma \leq 0.10$ and which are single counterparts of EPIC sources within a correlation radius of 4.0″. The intrinsic colours of dwarfs and giants (taken from Bessell & Brett 1988) are indicated by the dashed and solid lines respectively. The open pentagons correspond to stars with J magnitudes brighter than 10.0 (mostly moderately reddened early-type stars), whilst the crosses indicate fainter stars.

In principle, this diagram can be used to identify pre-main sequence stars (Lada & Adams 1992) either through a large circumstellar extinction characteristic of deeply embedded protostars or through infrared excesses produced by circumstellar disks in classical T Tauri stars (cTTs). The latter objects are expected to fall mostly to the right of the reddening band. Meyer et al. (1997) have shown that the locus of dereddened *JHK* colours of cTTs can be described by a simple linear relation between $J-H$ and $H-K$. This relation is shown in Fig. 4 by the dotted straight line. Only a modest number of the IR counterparts in Fig. 4 have colours that are consistent with these objects being surrounded by large amounts of circumstellar material. The majority of the secondary X-ray sources could thus be weak line T Tauri stars (wTTs) which display little or no evidence for circumstellar material in their spectra and photometry. This situation is strongly reminiscent of other young clusters such as NGC 6383 (Rauw et al. 2003) or NGC 6231 (Sana et al. 2007) where the X-ray selected pre-main sequence objects are also dominated by wTTs.

5. Variability

5.1. Short term variability

To study possible variations of the detected sources within individual data sets, we applied the following variability tests: (i) we computed χ^2 to test the null hypothesis of a constant count rate level in the data; (ii) we applied the Kolmogorov-Smirnov (KS) test to check if the statistics of the count rate follows a normal distribution; (iii) we used the so-called *probability of variability pov* test suggested by Preibisch & Zinnecker (2002) in its modified version suggested by Sana et al. (2004).

In all methods, the source data were extracted from circular regions with the radius equal to half of the distance to the nearest other source, or 60″ if no nearby sources were present. The first two methods were applied to the background-corrected light curves of every source produced by binning photons in time and energy (see below). Note that, for faint sources, the KS test can sometimes fail for the background-subtracted light curves. The third method was applied on the series formed by photon arrival times (the photons were still binned in the same energy bins as for the χ^2 test). Thus, when using the *pov* method, it was
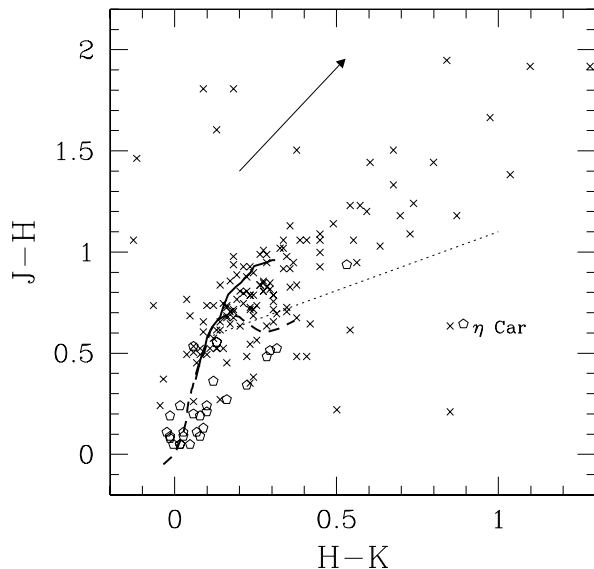

Fig. 4. JHK_s colour–colour diagram of the single IR counterparts falling within the 4.0″ correlation radius from an X-ray source. The heavy dashed and solid lines yield the intrinsic colours of main sequence and giant stars respectively, whereas the reddening vector is illustrated for $A_V = 5$ mag of visual extinction. Bright counterparts with $J < 10.0$ are displayed by open pentagons. The crosses indicate fainter IR sources. The dotted straight line yields the locus of dereddened colours of classical T Tauri stars according to Meyer et al. (1997).

not possible to account for the background. All variability tests were also applied to the background data.

To use the χ^2 and KS criteria, we produced light curves of the sources with various time bin sizes (from 10 to 5000 s) and in the soft S, medium M, hard H and total (0.4−10.0 keV) energy ranges. Since the Carina region is quite crowded, it was often impossible to find a source-free area in the vicinity of a given source to extract a background light curve. For this reason, we adopted the following scheme when extracting the background light curves. For the MOS instruments, the internal instrumental background is more or less constant within a single CCD. For the PN, the internal background primarily varies with the distance along the detector "y"-axis from the central detector "x"-axis (separating 2 sets of the PN CCDs). Thus, for the MOS instruments, we defined several object-free circular areas on every CCD and extracted one background light curve per energy range per MOS CCD from all these areas. The background light curves from a given MOS CCD were used for all objects located on that CCD. We performed a similar procedure with the PN background light curves except that circular background areas were selected in 10 strips parallel to the central PN "detx"-axis. Apart from instrumental background, there exists diffuse X-ray emission from the Carina nebula. Thus the background light curves obtained as above, may overestimate or underestimate the real background level near particular sources. This could influence the results for the faintest sources. However, in practice this is not very important as (i) we use several methods for detecting variability, including those without background subtraction; (ii) the count rates of the faintest sources are small anyway resulting in large errors and small chances to find variability; (iii) as the diffuse emission has large spatial scale (about the size of one CCD or larger) the adopted procedure roughly accounts for global changes of the diffuse background.

To increase signal, the sum of the background-corrected MOS1 and MOS2 light curves was also analysed whenever
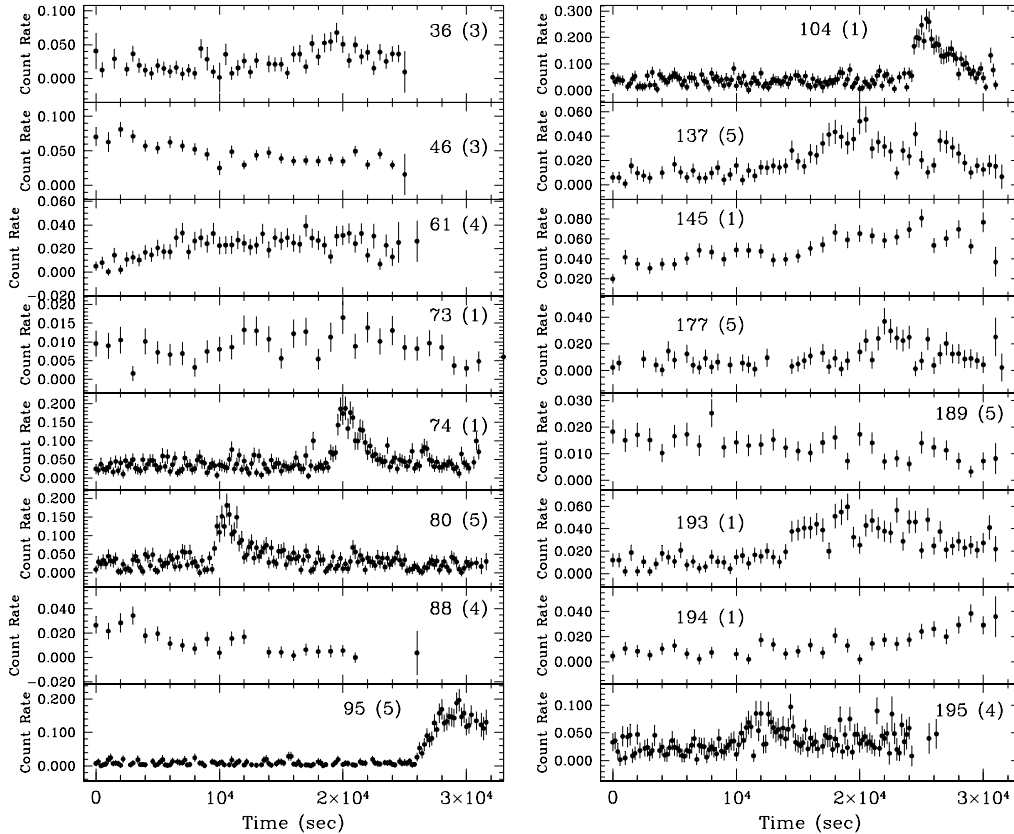
Fig. 5. PN background-subtracted light curves in counts s^{-1} of sources showing significant short term variability (MOS1 light curve for the source 73). The energy range is 0.4−10.0 keV. The source numbers followed by the data set numbers in parantheses are shown (for source identification see text and Table 3). In this and the following light curve plots (Figs. 6−8) the time shown is relative to the start of the exposure.

possible. In Fig. 5 we show the PN light curves of those objects for which the null hypothesis is rejected at a confidence level of 99% using all three variability test methods (for source 81 we show the MOS1 light curve as the source falls onto a gap between PN CCDs). We do not show the MOS1 and MOS2 light curves due to lack of space. The behaviour of these light curves is similar to the PN ones. The time bin sizes of the plots were selected according to typical variability time scales of the corresponding light curves.

Little is known about the nature of most of the variable sources. Only one source (#189) is identified with HD 93343 (O7 V(n)). The sources #36 (=MJ 156), #46 (=Tr 14 18), #104 (=DETWC-16 10,5), #145 (=Tr 14 Y 66), and #195 (=DETWC-16 345) are identified with the 2MASS and optical catalogues but no spectral type is known. The sources #74, 80, 115, 137, 177, 194 are identified with the 2MASS catalogue, no optical identification is known. The sources #61, 73, 88, 95, 193 are not identified with any optical or IR catalogues. All the sources displayed show variability at different levels, and 3 of them (#74, 80 and 104) are clearly flaring.

5.1.1. The probable pre-main sequence stars #74, #80, and #104

Further insight into the nature of the flare-type sources may be obtained from the analysis of their light curves and spectra during the flare events. But first, let us consider the IR properties of the flaring X-ray sources.

Figure 9 illustrates the K vs. $J − K$ colour−magnitude diagram of the 2MASS counterparts in the EPIC field of view. We

used the March 2003 update of the colour transformations, initially derived by Carpenter (2001) and available on the 2MASS website[2], to convert the 2MASS colours and magnitudes into the homogenized *JHK* photometric system introduced by Bessell & Brett (1988).

Assuming all the sources are at the same distance, the sources to the right of the main sequence could indicate the existence of a population of pre-main sequence stars. The counterparts of three flaring X-ray sources are illustrated by the triangles (solid triangles stand for the two possible counterparts of source #104, whilst the open triangles show sources #74 and #80). The flaring X-ray sources with single 2MASS counterparts are clearly located at positions consistent with these objects being PMS stars.

The X-ray light curves of the three flaring sources are shown in Figs. 6−8. It is immediately evident that the flares occur mostly in the hard energy range which is consistent with these observed flares being produced by the coronal activity in PMS stars.

Assuming that the plasma producing the observed variabiltiy is confined in a closed coronal loop as is the case for solar flares, we can use the method proposed by Serio et al. (1991). These authors established an analytical relation between the loop half-length l, the maximum temperature at the top of the loop T_{max} and the thermodynamic decay time τ (see also Briggs & Pye 2003; Giardino et al. 2004; and Favata 2005).

We have determined the $1/e$ decay times of the flares of sources #74, 80 and 104 by a least square fit of the exponential

---

[2] http://www.ipac.caltech.edu/2mass/index.html
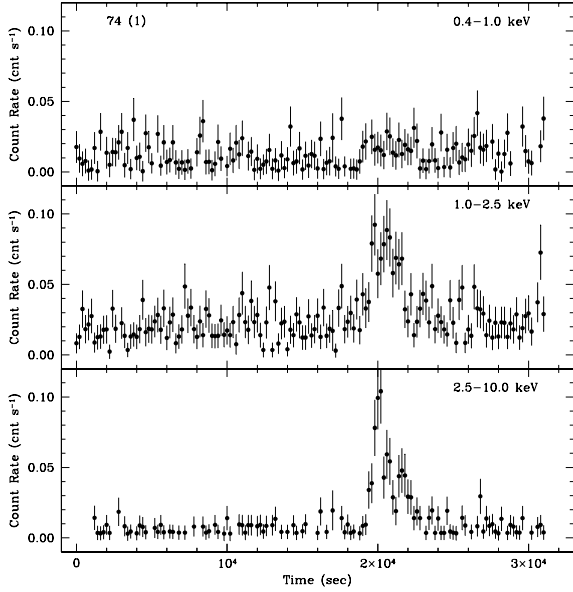
Fig. 6. PN light curves of source #74 in the soft, medium, and hard energy bands.
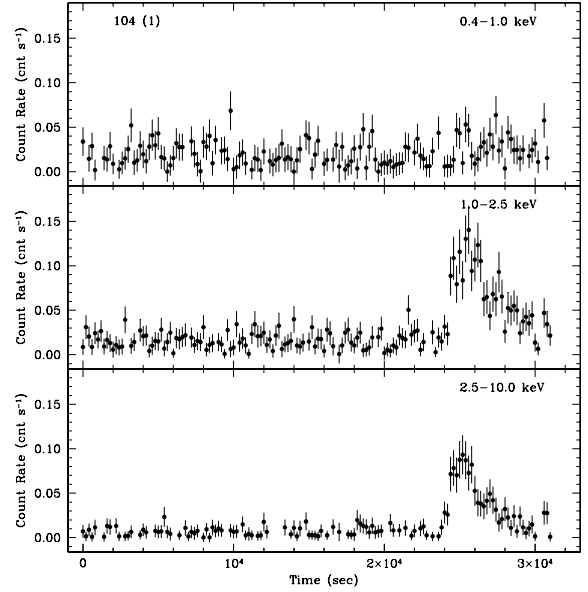
Fig. 8. PN light curves of source #104 = DETWC-16 10,5 (data set 1) in the soft, medium, and hard energy bands.
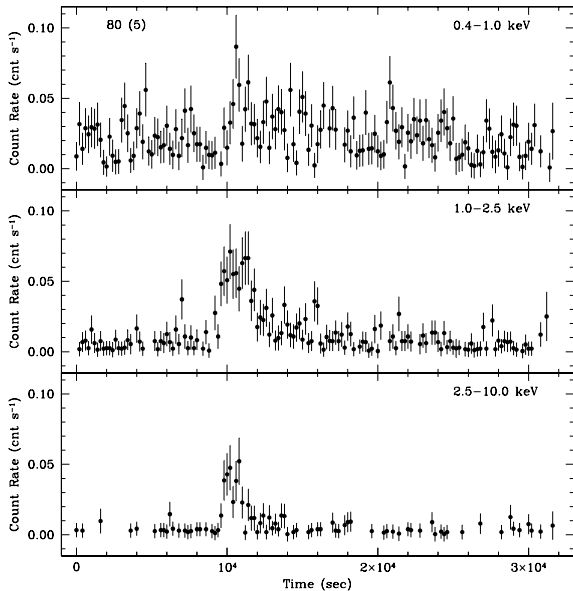
Fig. 7. PN light curves of source #80 in the soft, medium, and hard energy bands.

Fig. 9. K vs. $J - K$ colour–magnitude diagram of the 2MASS counterparts with good quality near-IR photometry of the X-ray sources in the EPIC field of view. The open pentagons indicate early-type stars, whilst the triangles stand for flaring X-ray sources. The locus of the un-reddened main sequence is indicated for a distance modulus of 12.0 by the leftmost solid line. The reddened main sequence is indicated for two different reddening values $A_V = 5$ (middle solid line) and $A_V = 10$ (rightmost solid line).

decay phase of the observed light curves. Considering the typical count rates of the sources studied here, the most useful time bins to study the light curves are 500 and 200 s for the MOS and PN data respectively. The decay times derived from the fits of the different EPIC light curves agree within 20%. The results are given in Table 4. All three sources have rather short decay times indicating that the X-ray emitting loops must be relatively compact. We fitted the spectra of the sources during the flare with an absorbed single temperature apec model. The best-fit column densities of the three sources are found to be $0.26-0.39 \times 10^{22}$ cm^{-2}. The best-fit temperatures are quite high ($kT \geq 4.2$ keV) as expected for pre-main sequence stars. The measured decay time of the flare actually exceeds the intrinsic thermodynamical decay time due to the effect of heating that can extend into the decay phase of the flare. The relation between the two $F(\zeta) = \tau_{\rm obs}/\tau_{\rm th}$ can in principle be determined from

the slope ζ of the flare decay in a $\log T - \log \sqrt{EM}$ diagram (Favata et al. 2005). Unfortunately, the flaring sources discussed here were too faint to allow a time-resolved spectral analysis. Therefore, we can only determine $l \times F(\zeta)$. For flaring loops that are freely decaying with no heating, $F(\zeta) \simeq 2$ (Favata et al. 2005) which actually represents the lower limit on $F(\zeta)$. Therefore, the typical loop sizes of the three sources are $\leq 0.55\,R_\odot$ (see Table 4).

Table 4. Properties of the flaring sources.

Source	Rev.	τ (ks)	kT_{obs} (keV)	$l \times F(\zeta)$ ($R_\odot$)	f_X (0.4–10 keV) (erg cm^{-2} s^{-1})	$J - K$	K
74	115	1.5 ± 0.3	13.3 ± 7.5	1.1 ± 0.3	9.3×10^{-13}	1.452	14.198
80	285	2.5 ± 0.6	4.2 ± 1.1	0.9 ± 0.2	2.9×10^{-13}	1.381	12.718
104	115	2.1 ± 0.4	4.6 ± 0.7	0.8 ± 0.1	9.1×10^{-13}		

τ yields the $1/e$ decay time, kT_{obs} is the best fit plasma temperature during the flare and l is the loop half-length. The X-ray fluxes correspond to the spectrum during the flare.

5.2. Set-to-set variability

To detect possible variability of the X-ray sources between the data sets we performed a χ^2 test at three different confidence levels (90, 95 and 99%) to test the null hypothesis of a constant count rate level in the data. The tests were performed for the count rates in the soft S, medium M, hard H, and total (0.4–10.0 keV) energy bands as well as for the hardness ratios HR_1 and HR_2, for all EPIC instruments. The results of the test are included in Table 2 (second column). The variability status is assigned as follows. If the null hypothesis is rejected at a confidence level of 95% in the total energy range in all instruments simultaneously, the source is labeled "Var". If the null hypothesis cannot be rejected in all instruments, the source is labeled "Const". If the null hypothesis is rejected in some instruments only, the variability status is set to "Uncert". Finally, if there is not sufficient data to perform the test, the variability status is set to "NoInfo".

Of course, given the limited number of data sets, the detected variabiltiy of a source tells us hardly more than the mere fact that the source is variable on a time scale of one day or one year (the time intervals between our data sets). The nature of this variability for the majority of the sources remains uncertain. The purpose of this test was to set a preliminary base for future studies. Some sources like HD 93205 (#117) are early-type binaries, in which case the X-ray flux varies with the orbital motion. Spectral analysis may help in disentangling the nature of the detected sources and their variability. Such an analysis will be the subject of forthcoming papers.

6. X-ray properties of early-type stars

We extracted the spectra of all early-type stars detected in the images, using the same apertures as for their light curves. The background spectra were extracted from circular apertures chosen in source-free areas as close as possible to the sources under investigation, so that the diffuse background emission is similar to that at a source position. The corresponding redistribution matrices and ancillary response files were generated for every source, the spectra were rebinned so that they contain a minimum of 10 counts per channel.

6.1. Spectral models

Table 5 lists all detected early-type stars along with the parameters of the spectral fits. Spectral fitting was generally performed for all data sets and all instruments MOS1, MOS2, and PN simultaneously. In some cases when a source was variable or the data from some instruments in a particular data set were affected by the CCD gaps, a subset of the data was used. To quantify the physical properties of the X-ray emission we adjusted a series of optically thin thermal plasma `apec` models to the observed

spectra using `xspec`. The general form of a multi-temperature model was `wabs`$_1$`*(apec`$_1$`+wabs`$_2$`*apec`$_2$`+...)`. `wabs`$_1$ is an absorption model using the cross-sections for cosmic abundances. We required that the column density of neutral hydrogen for this model component was not smaller than the value given in the 5th column of Table 5. The column density was calculated individually for every star using the empirical relation from Bohlin et al. (1978). Additional `wabs` components account for possible internal absorption of X-ray radiation in the winds of early-type stars. Metal abundances were fixed to the solar value in all cases except WR 25, in which case it was a free parameter. In a few cases a Fe line complex (or indication of it) was present in the spectra at 6.4–6.8 keV. This line complex may include the Fe I fluorescence line at ~6.4 keV and the lines of Fe XXV and XXVI centered around 6.7 keV. The potential presence of the Fe I line (indicative of cool material) may skew the high temperature model component required to fit the Fe XXV and XXVI lines. We did a check for the presence of the Fe I line as follows. We start fitting with just one thermal model component and include a Gaussian component at 6.4 keV. If necessary, we increase the number of thermal components until a satisfactory fit is achieved. We then remove the Gaussian component and check if the goodness of fit decreases significantly. If not, we permanently remove this component from the model. It turned out that no significant Fe I emission was found in any sources.

Table 5 does not include the brightest object in the FOV, η Car. The nature of this star is so complicated that it makes little sense to give the results of a necessarily superficial analysis here. A detailed study of *XMM-Newton* observations of this star was recently published by Hamaguchi et al. (2007). A few weak OB stars were also excluded from the table as no reliable spectral fits could be performed.

The number of thermal components for different sources varies from one to three. Spectra of some stars required rather high temperature model components. Below we will discuss possible reasons for this. We also tried to fit the spectra with combinations of thermal and power law models. These did not result in better fits. Note that for some weak sources, the fitted parameters are not really well constrained and about the same quality of the fit can be obtained in a single-temperature model for different combinations of N_H and kT. However, as we are most interested in the source *fluxes* within the *XMM-Newton* energy range, the somewhat formal fits are acceptable. Our model parameters are roughly in agreement with those obtained by AC03 and EV04 (the latter are based on a Chandra observation of the region). The exact comparison is impossible as we used somewhat different models (e.g. different number of temperatures in thermal models), owing to different quality of the data.

A few examples of the observed spectra along with the fitted models are shown in Figs. 10–13. These examples show WR 25 and some OB stars of different brightness, to illustrate the quality of the data.

Table 5. Parameters of spectral fitting for early type stars in the Carina Nebula.

X#	Source name	Spectral type	$E(B-V)$	$N_{\mathrm{ISM}}^{\mathrm{H}}$ $(10^{22}\,\mathrm{cm}^{-2})$	N_{H} $(10^{22}\,\mathrm{cm}^{-2})$	kT (keV)	Norm (10^{-4})	χ^2/d.o.f.	d.o.f.
26	MJ 126	B2 Vb	0.42	0.24	$0.24^{+0.06}_{-0.00}$	$0.67^{+0.06}_{-0.07}$	$0.49^{+0.12}_{-0.07}$	1.14	135
30	CPD-58°2611	O6 V((f))	0.45	0.26	$0.76^{+0.11}_{-0.12}$	$0.54^{+0.07}_{-0.07}$	$0.89^{+0.29}_{-0.25}$	1.69	51
33	Tr 14 21	O9 V	0.61	0.35	$1.21^{+0.14}_{-0.14}$	$0.19^{+0.06}_{-0.06}$	$44.1^{+41.0}_{-41.0}$	1.45	225
					$0.00^{+0.38}_{-0.00}$	$2.19^{+0.22}_{-0.21}$	$2.30^{+0.47}_{-0.47}$		
45	HD 93129 A+B	O3 Iab...+O3.5 V	0.56	0.32	$0.77^{+0.07}_{-0.06}$	$0.14^{+0.01}_{-0.02}$	392^{+870}_{-168}	1.11	1191
					$0.16^{+0.06}_{-0.03}$	$0.50^{+0.03}_{-0.02}$	$33.2^{+3.6}_{-3.9}$		
					$0.68^{+0.22}_{-0.17}$	$1.78^{+0.13}_{-0.13}$	$11.6^{+1.4}_{-1.3}$		
46	Tr 14 18[†]	B0 V	0.52	0.30	$0.30^{+0.05}_{-0.00}$	$2.43^{+0.18}_{-0.20}$	$2.36^{+0.15}_{-0.12}$	1.22	185
51	HD 93130	O6 III(f)	0.48	0.28	$0.28^{+0.02}_{-0.02}$	$0.58^{+0.02}_{-0.02}$	$0.68^{+0.05}_{-0.04}$	1.13	263
59	Tr 16 124	B1 V	0.50	0.29	$0.29^{+0.06}_{-0.00}$	$2.30^{+0.42}_{-0.31}$	$0.46^{+0.05}_{-0.05}$	1.16	101
63	HD 93160	O6 III(f)	0.31	0.18	$0.58^{+0.09}_{-0.07}$	$0.25^{+0.03}_{-0.02}$	$6.68^{+3.38}_{-1.67}$	0.99	258
					$0.35^{+0.39}_{-0.35}$	$1.25^{+0.69}_{-0.24}$	$0.66^{+0.36}_{-0.21}$		
67	HD 93161A+B	(O8 V+O9 V)+O6.5 V(f)	0.29	0.17	$0.57^{+0.08}_{-0.06}$	$0.27^{+0.03}_{-0.03}$	$7.36^{+5.63}_{-1.20}$	1.05	342
					$0.61^{+0.57}_{-0.32}$	$1.16^{+0.39}_{-0.24}$	$0.81^{+0.31}_{-0.22}$		
71	HD 93162 (WR 25)[†][†]	WN6h	0.69	0.40	$0.59^{+0.09}_{-0.09}$	$0.46^{+0.12}_{-0.08}$	$16.0^{+4.8}_{-6.4}$	1.05	1017
					$0.29^{+0.13}_{-0.10}$	$0.75^{+0.06}_{-0.03}$	$51.6^{+9.0}_{-9.6}$		
					$0.00^{+0.06}_{-0.00}$	$2.46^{+0.15}_{-0.06}$	$35.0^{+2.7}_{-3.6}$		
108	CPD-58°2649	B0 V	0.54	0.31	$0.78^{+0.11}_{-0.14}$	$0.15^{+0.06}_{-0.03}$	$21.5^{+96.6}_{-19.3}$	1.02	92
					$0.00^{+0.44}_{-0.00}$	$2.39^{+1.70}_{-0.65}$	$0.24^{+0.07}_{-0.05}$		
110	HD 93204	O5 V((f))	0.39	0.23	$0.34^{+0.18}_{-0.11}$	$0.18^{+0.06}_{-0.03}$	$2.44^{+11.1}_{-1.70}$	1.18	239
					$0.09^{+0.16}_{-0.09}$	$0.59^{+0.04}_{-0.04}$	$0.91^{+0.12}_{-0.14}$		
117	HD 93205	O3.5 V+O8 V	0.40	0.23	$0.42^{+0.04}_{-0.15}$	$0.18^{+0.02}_{-0.01}$	$10.8^{+4.5}_{-10.4}$	1.13	524
					$0.03^{+0.13}_{-0.01}$	$0.58^{+0.02}_{-0.02}$	$3.20^{+0.28}_{-0.35}$		
126	HDE 303311	O5 V	0.44	0.26	$0.26^{+0.09}_{-0.00}$	$0.29^{+0.02}_{-0.04}$	$0.81^{+0.69}_{-0.08}$	1.05	238
					$0.00^{+0.28}_{-0.00}$	$1.82^{+0.43}_{-0.40}$	$0.27^{+0.07}_{-0.04}$		
135	CPD-59°2600	O6 V((f))	0.48	0.29	$0.29^{+0.02}_{-0.00}$	$0.60^{+0.02}_{-0.03}$	$1.01^{+0.08}_{-0.26}$	1.11	275
					$0.00^{+2.51}_{-0.00}$	$4.84^{+23.4}_{-2.35}$	$0.16^{+0.22}_{-0.06}$		
142	HD 93250	O3 V	0.48	0.29	$0.29^{+0.02}_{-0.02}$	$0.31^{+0.02}_{-0.02}$	$4.30^{+0.73}_{-0.32}$	1.01	1408
					$0.31^{+0.06}_{-0.05}$	$0.74^{+0.03}_{-0.02}$	$6.66^{+1.17}_{-0.82}$		
					$0.00^{+0.03}_{-0.00}$	$3.05^{+0.21}_{-0.15}$	$6.82^{+0.36}_{-0.46}$		
147	CPD-59°2603	O7 V+O9.5 V+B0.2 IV	0.43	0.25	$0.26^{+0.21}_{-0.01}$	$0.32^{+0.03}_{-0.03}$	$0.37^{+0.82}_{-0.32}$	1.20	165
			0.43	0.25	$0.42^{+0.17}_{-0.14}$	$0.69^{+0.09}_{-0.09}$	$0.32^{+0.20}_{-0.20}$		
178	CPD-59°2626	O7 V	0.65	0.38	$0.46^{+0.50}_{-0.08}$	$0.23^{+0.06}_{-0.06}$	$1.19^{+6.60}_{-1.19}$	1.11	55
					$0.63^{+0.35}_{-0.34}$	$0.84^{+0.21}_{-0.20}$	$0.79^{+0.59}_{-0.59}$		
179	HDE 303308[†][††]	O3 V((f))	0.44	0.26	$0.60^{+0.05}_{-0.09}$	$0.12^{+0.03}_{-0.01}$	171^{+116}_{-123}	1.13	632
					$0.00^{+0.06}_{-0.00}$	$0.48^{+0.05}_{-0.04}$	$4.79^{+0.95}_{-1.00}$		
					$3.88^{+0.49}_{-0.44}$	$3.80^{+0.44}_{-0.43}$	$0.15^{+0.02}_{-0.02}$		
183	CPD-59°2629	O8.5 V	0.78	0.45	$0.86^{+0.06}_{-0.07}$	$0.29^{+0.03}_{-0.02}$	$9.18^{+3.43}_{-2.82}$	0.96	924
					$0.15^{+0.13}_{-0.13}$	$1.92^{+0.13}_{-0.12}$	$3.16^{+0.27}_{-0.23}$		
189	HD 93343	O7 V(n)	0.54	0.31	$0.63^{+0.13}_{-0.12}$	$0.29^{+0.04}_{-0.05}$	$2.45^{+1.61}_{-1.14}$	1.33	159
					$0.01^{+1.14}_{-0.01}$	$2.81^{+1.49}_{-1.40}$	$0.47^{+0.36}_{-0.08}$		
191	CPD-59°2636	O7 V+O8 V+O9 V	0.56	0.32	$0.51^{+0.03}_{-0.06}$	$0.56^{+0.04}_{-0.06}$	$1.37^{+0.39}_{-0.25}$	1.30	120
197	CPD-59°2641	O6 V((f))+?	0.58	0.34	$0.54^{+0.08}_{-0.07}$	$0.64^{+0.08}_{-0.05}$	$0.95^{+0.23}_{-0.23}$	1.12	102
218	MJ 596	O5 V((f))+O9.5 V	0.73	0.42	$0.53^{+0.24}_{-0.11}$	$0.56^{+0.13}_{-0.13}$	$0.54^{+0.69}_{-0.37}$	1.21	160
					$0.95^{+1.64}_{-0.79}$	$2.65^{+1.15}_{-0.98}$	$1.13^{+1.02}_{-0.40}$		
235	HDE 303304	O+...	0.61	0.35	$0.54^{+0.12}_{-0.11}$	$0.18^{+0.02}_{-0.02}$	$11.0^{+17.4}_{-10.1}$	0.96	107

$N_{\mathrm{ISM}}^{\mathrm{H}}$ is the ISM column density of neutral hydrogen. Norm is the normalization factor of a thermal model component given by Norm = $\frac{10^{-14}}{4\pi d^2}\int n_{\mathrm{e}}n_{\mathrm{H}}\mathrm{d}V$, where d is the distance to the source (cm), n_{e} and n_{H} are the electron and H densities (cm^{-3}).
[†] – Parameters may be unreliable as the star is located in an area of extremely varying background and close to a cluster of bright stars.
[†][†] – Metal abundance 0.59 ± 0.07.
[†][††] – Parameters may be unreliable due to proximity to η Car and a strong non-uniform background.

6.2. X-ray fluxes and L_x/L_{bol} ratio

The X-ray absorbed and unabsorbed (i.e. corrected for the interstellar absorption) fluxes and bolometric luminosities of OB stars detected in the *XMM-Newton* data are presented in Table 6. The first column is the source number, the second to fifth columns are the absorbed X-ray fluxes in the soft, medium, hard, and total energy bands, while the following four columns are the unabsorbed fluxes in the same bands. The tenth column is the bolometric magnitude.
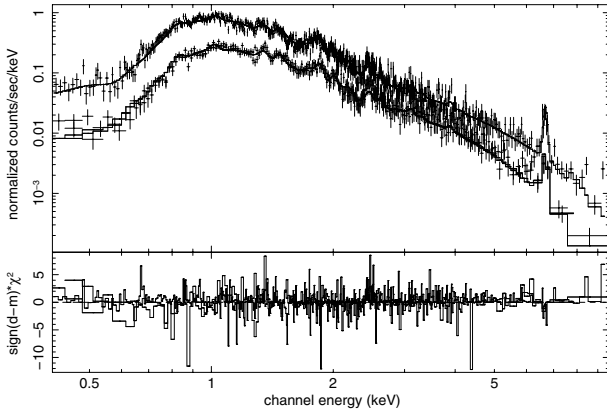
Fig. 10. EPIC spectra of WR 25 from the data set 3 along with the best-fit model. In the top panel, the upper and lower data correspond to the PN and MOS spectra, respectively, and the solid lines yields the best-fitting model. The bottom panel shows the contribution of individual energy bins to the χ^2 of the fit.
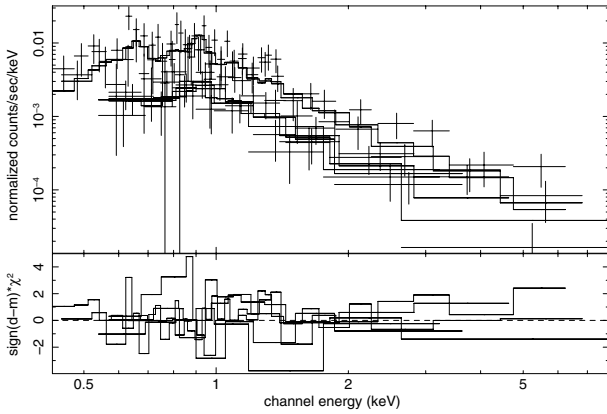
Fig. 11. Example of a weak source. EPIC spectra of the source #108 (CPD-58°2649) from the data sets 4 and 5.

EV03 thoroughly discuss bolometric magnitudes for the early type stars they detected in their Chandra data. We adopted their bolometric magnitudes for the sources in common. For the stars not detected in the Chandra data, we, like EV03, compute the bolometric magnitudes using the approach and formulae from Massey et al. (2000). Briefly, the reddening $A_V = R \times E(B - V)$ with $R = 3.2$ was computed for each star to get its de-reddened visual magnitude. The bolometric correction of a star was computed using the relationship $BC = 27.66 - 6.84 \times \log T_{\mathrm{eff}}$. In the complex case of HD 93161 consisting of three components Aa, Ab, and B, we computed the bolometric luminosities of every component separately using the information about the colors and temperatures from Nazé et al. (2005) and then summed them up to get the total bolometric luminosity of the system. For MJ 596 we used the bolometric magnitude obtained by Niemela et al. (2006) from the detailed analysis of spectral and photometric data.

Figure 14 shows the intrinsic L_X versus L_{bol} for the stars in Table 6, in every energy band. It is known from the literature (e.g. S06) that O- and B-type stars show a different behaviour. For this reason we marked them with different symbols. Presumed single O-type stars are marked with solid circles, binary stars are plotted as solid triangles, and B-type stars are marked with open circles. The demarcation line between two types of stars is located at about $L_{\mathrm{bol}} = 10^{38}$ erg s^{-1}. We shall not discuss B-type stars here as their number in our sample is small.
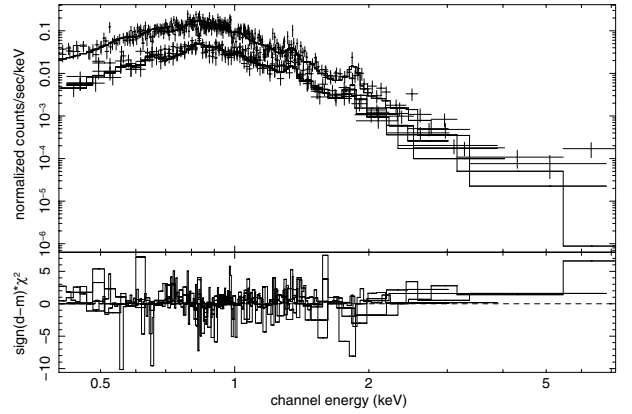
Fig. 12. EPIC spectra of the source #117 (HD 93205) from the data sets 4 and 5.
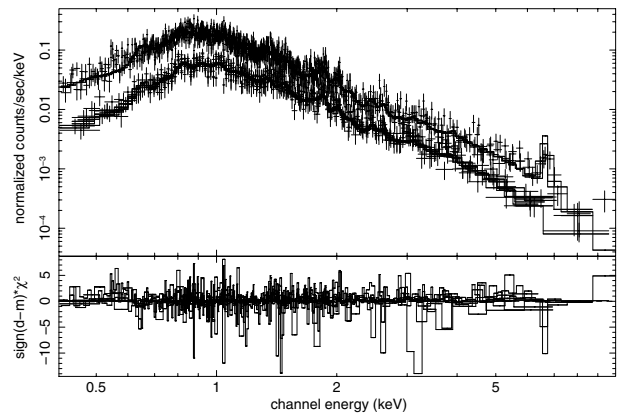
Fig. 13. EPIC spectra of the source #142 (HD 93250) from the data sets 3−5. Note the presence of the Fe line complex at 6.4−6.7 keV.

The X-ray and bolometric luminosities of O-type stars are clearly correlated in the soft and medium bands. In the hard band the errors are large so no definite conclusion can be drawn.

The solid lines in Fig. 14 represent the least-square fits of the observed distributions of O-type stars (both binary and single) in the form

$$\log(L_X) = a + \log(L_{\mathrm{bol}})$$

which represents a simple scaling relation $L_X = 10^a \times L_{\mathrm{bol}}$. Our data do not allow us to search for a more sophisticated relation e.g. in the form of a power law.

As seen from Fig. 14, there is no clear distinction between binary and single O-type stars in the L_X–L_{bol} plane. We performed various tests on the two samples taken separately. It turned out that the correlation coefficients for the two samples, the parameters of the least square fits, and the fit residuals were all very close. The numerical values of the least-square unweighted fit parameters for the whole (single plus binary) sample of O-type stars are:

$$\log(L_X^{\mathrm{soft}}) = (-6.82 \pm 0.56) + \log(L_{\mathrm{bol}})$$

$$\log(L_X^{\mathrm{med}}) = (-7.18 \pm 0.92) + \log(L_{\mathrm{bol}})$$

$$\log(L_X^{\mathrm{total}}) = (-6.58 \pm 0.79) + \log(L_{\mathrm{bol}}). \tag{1}$$

The errors of the parameter are obtained *assuming* a good fit (Press et al. 1992) and are rather formal. The dispersion of the

Table 6. X-ray fluxes and absolute magnitudes of early type stars in the Carina Nebula.

X#	Absorbed Flux				Unabsorbed Flux				M_{bol}
	[0.4–1.0]	[1.0–2.5]	[2.5–10.0]	[0.4–10.0]	[0.4–1.0]	[1.0–2.5]	[2.5–10.0]	[0.4–10.0]	
26	3.52	2.43	1.37	6.09	9.12	3.40	0.142	12.66	−6.21
30	0.86	1.74	0.10	2.71	2.22	2.41	0.104	4.74	−6.30
33	1.28	7.22	8.65	17.1	4.88	9.94	8.92	23.72	−5.95
45	32.4	74.5	33.5	140.4	151.5	105.8	34.6	291.8	−11.5
46	1.80	11.0	11.0	23.8	8.57	14.81	11.30	34.7	−3.86
51	4.00	2.66	0.11	6.77	12.7	3.99	0.12	16.8	−8.83
59	0.369	2.18	1.98	4.53	1.68	2.92	2.03	6.63	−5.76
63	4.91	4.58	0.94	10.4	11.0	5.75	0.96	17.7	−9.4
67	6.71	5.91	0.97	13.6	14.0	7.36	0.99	22.4	−9.39
71	46.9	216.1	150.0	413.0	205.0	324.9	155.5	685.4	−10.1
108	1.23	1.18	1.07	3.48	6.40	1.67	1.10	9.17	−6.9
110	5.99	3.29	0.16	9.43	20.6	4.51	0.16	25.2	−9.0
117	18.2	11.4	0.52	30.0	58.1	15.5	0.55	74.2	−10.1
126	3.34	2.26	0.84	6.44	13.4	3.17	0.86	17.4	−8.6
135	5.90	4.76	1.66	12.3	19.4	7.04	1.69	28.1	−9.0
142	32.8	59.0	44.0	135.8	124.0	81.5	45.0	250.5	−10.7
147	2.02	1.45	0.10	3.55	6.60	2.02	0.10	8.72	−8.5
178	1.62	2.35	0.40	4.36	11.3	3.60	0.42	15.3	−7.5
179	15.9	17.7	89.6	123.2	70.6	23.0	90.9	184.5	−9.8
183	3.00	12.4	9.88	25.3	18.2	19.8	10.3	48.2	−6.8
189	1.97	3.03	2.57	7.54	7.48	4.36	2.63	14.3	−8.0
191	3.39	3.87	0.20	7.46	11.6	5.99	0.21	17.8	−8.3
197	2.23	3.02	0.22	5.47	7.71	4.68	0.23	12.6	−8.7
218	1.27	3.63	5.41	10.3	6.47	5.45	5.58	17.5	−8.18
235	4.53	1.08	0.001	5.61	35.2	1.88	0.0012	37.1	−7.45

Fluxes are in units 10^{-14} erg cm^{-2} s^{-1}.

luminosities around Eqs. (1) are 29%, 48%, and 41% in the three bands above.

In the soft and medium bands, a few O-type stars deviate from the least-square scaling relation more than the others. These stars are labeled with their names in Fig. 14. There is no unique reason for this deviation. HDE 303304 shows increased X-ray luminosity in the soft band. The star is somewhat unusual; it is classified as "OB+(le)" (that is having at least one emission line in its spectrum) by Stephenson & Sanduleak (1971). It is not clear if this can be related to the increased luminosity in the soft band. On the other hand, the binary hypothesis is not very likely. If the increased X-ray flux is due to wind-wind collision, then the X-ray spectrum should also be *harder* than a typical spectrum of a single star, and thus the X-ray limunosities in the medium and hard X-ray bands ought to be higher than average. Evidently this is not the case. More likely is that the soft X-ray flux of HDE 303304 is affected by the diffuse background X-ray emission. The source is weak and the diffuse X-ray emission has maximal flux in the soft X-ray band. It is also very inhomogeneous across the field of view.

The O8.5 V star CPD -59°2629 (=Tr 16 22) is also discovered as an unusually bright and hard X-ray source for its spectral type by Chandra instruments (EV04). The latter authors suggested that the unusually large L_X/L_{bol}, as well as a surprisingly hard spectrum, could indicate the presence of a wind confined by the magnetic fields of this star. Another possible explanation could be the presence of a low-mass pre-main sequence companion. These objects can have L_X/L_{bol} up to 0.001 and even 0.01 (during flares). However, in the absolute terms, it is unlikely that they would be bright enough to be seen against the intrinsic X-ray emission of an early-type star. E.g., In NGC 6231, PMS stars can typically display L_X up to 10^{31} erg s^{-1} (Sana et al. 2007).

The deviations in the soft and medium bands of Tr 14 21 is likely related to the fact that this weak source is located near the edge of the field of view, in an extremely crowded area with strong and variable background diffuse emission.

Despite the fact that some deviations from the least-square scaling relations in Fig. 14 could be understood as instrumental effects we did not exclude the corresponding stars from the fits. The reason is that, even for stars which are visually "well-behaved", the uncertainies in the exact value of the diffuse background emission, and especially in the inferred neutral hydrogen column densities, may still be important factors influencing the exact location of the data points in Fig. 14. We believe that excluding the deviating points for the sole purpose of getting a nicer-looking plot is not a good approach in this case.

6.3. Comparison with X-ray fluxes from other reviews

Before we turn to the discussion of the results let us briefly check the consistency of the fluxes obtained in the current study, with the previous values presented in EV03 and AC03.

First, note that five OB stars from the list of EV03 (#8, 9, 39, 44, 141) are not detected in our *XMM-Newton* data, even despite the fact that the effective telescope area and exposure times are larger in the *XMM* case. This is explained by the lower spatial resolution of *XMM*. All these stars are weak X-ray sources. Stars #8 and #9 are located near the brightest object in the region – η Car (about 39″ and 57″ respectively), and are lost in the bright background created by the Homunculus. The EV03 source #44 is between the *XMM* close sources #189 and #191, the EV03 source #141 is very weak and is located near another XMM source #90. As a consequence, these sources were not detected by the SAS detection routine.
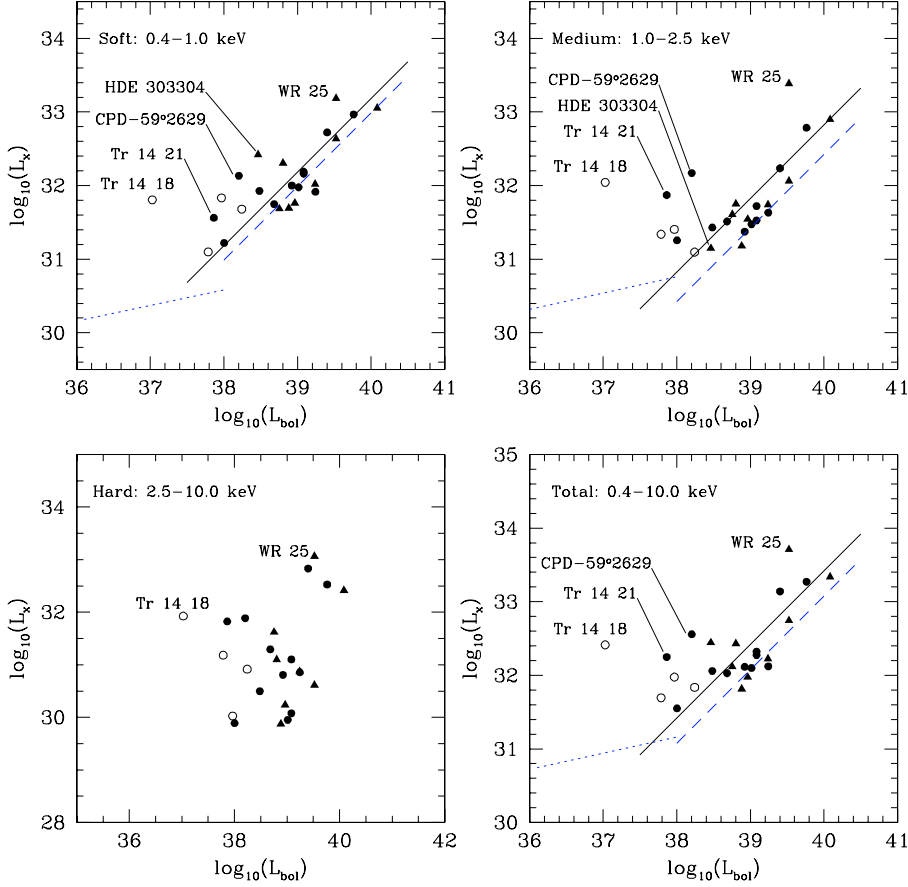
Fig. 14. L_X versus L_{bol} for early-type stars in the Carina Nebula in different energy bands. B-type stars and WR 25 are excluded from the least-square fits. The dashed and dotted lines show the best-fit approximations of the $L_X - L_{bol}$ relation for O (dashed lines) and B (dotted lines) stars in NGC 6231 (Sana et al. 2006, hereafter S06).
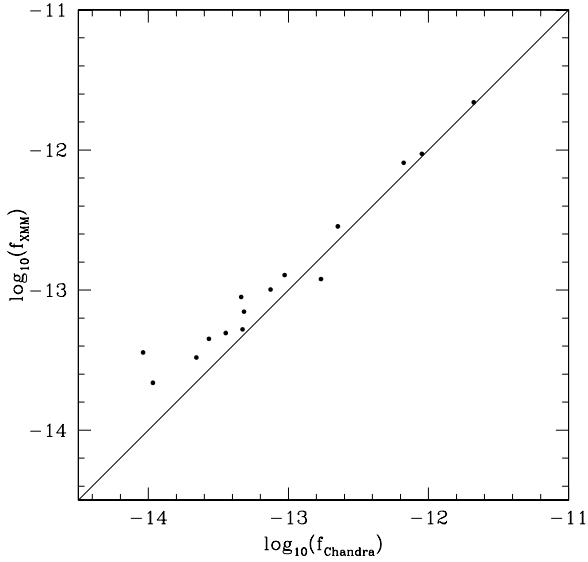
Fig. 15. Comparison of absorbed *XMM-Newton* and Chandra fluxes in the energy band 0.5−2.04 keV.

Fig. 16. Comparison of absorbed fluxes from the current study (energy band 0.4−10.0 keV) and the study of AC03 (energy band 0.3−12.0 keV).

A comparison of absorbed *XMM* and Chandra fluxes for common early-type sources is shown in Fig. 15. EV03 computed their unabsorbed Chandra fluxes in the energy band 0.5−2.04 keV from the observed count rates assuming a single-temperature plasma model with the temperature $kT = 0.385$ keV and the hydrogen column density $N_H = 0.3 \times 10^{22}$ cm^{-2}. We converted these fluxes (taken from the Table 3 of EV03) to the absorbed ones using the above model parameters. *XMM-Newton* absorbed fluxes were computed in the same energy band 0.5−2.04 keV using the best-fit models from Table 5. The results of the two telescopes are in quite good agreement, especially accounting for the calibration issues at the time of Chandra observation.

A comparison of absorbed fluxes of early-type stars from the current study with the fluxes from AC03 (their Table 3) is shown in Fig. 16. Two weak stars with problematic fluxes (our #179 and #197) are excluded from the plot. The AC03 fluxes are computed in the energy range $0.3 - 12$ keV which explains the systematic shift between our and their fluxes. Otherwise, the agreement is quite good.

7. Discussion

7.1. General properties of the field

The X-ray images of the Carina region are dominated by diffuse emission and strong discrete sources. The brightest discrete sources are associated with the hot massive stars in the various clusters that populate this region (see Sect. 4). Among the fainter sources, there are likely some extragalactic background objects, but the vast majority are likely to be low-mass stars, either foreground coronal sources or pre-main sequence stars in the Carina complex (see Sect. 5.1.1). Compared to some other open clusters such as NGC 6231, there are less PMS candidates detected. This could be due to a lower detection efficiency (due to the strong diffuse emission) and the larger distance of the Carina complex compared to NGC 6231.

7.2. Early-type stars

In Sect. 6.1 we derived the spectral characteristics and the observed $L_X - L_{bol}$ relations for O-type stars in our sample. Recently, a similar investigation was published regarding the early-type population in NGC 6231 by S06. The authors also provide a review of the previous works on this subject. The S06 linear fits of the $L_X - L_{bol}$ relations for O and B stars in NGC 6231 are shown in Fig. 14 by dashed and dotted lines respectively.

When comparing our results with those of S06 one should keep in mind that the Carina Nebula is known as a region with very patchy interstellar absorption, thanks to numerous arms of dust and gas penetrating through the volume of the stellar associations. For this reason it is extremely difficult to account accurately for the ISM absorption. The situation with NGC 6231 is less complex and this is a probable explanation for the scatter of data points in our Fig. 14 which is somewhat larger than in the case of S06[3]. In addition, the difficulty with the ISM absorption may also influence the accuracy of the bolometric luminosities of the stars under investigation.

The numerical parameters of the S06 scaling relations are generally similar to ours: e.g. for their full sample of O-type stars and in the total energy band $0.4 - 10.0$ keV their $\log{(L_X/L_{bol})} = -6.865 \pm 0.186$ (cf. our value for the $0.4 - 10.0$ keV band: -6.58 ± 0.79).

The biggest difference between Sana et al. and our values of the scaling parameter for O-type stars is in the medium band. It is explained by the fact that in our fits we included all O-type stars while S06 provide the best fit value for a sub-sample of O-type stars excluding two deviating binary systems. If we exclude two anomalous stars Tr 14 21 and CPD$-59°$ 2629 from the medium band fit, the scaling parameter changes from -7.18 to -7.32, a value closer to the one of Sana et al. (-7.58 ± 0.2). Our results on the $L_X - L_{bol}$ relation can be summarised as follows:

1. The canonical relation $L_X \sim 10^{-7} \times L_{bol}$ is mainly defined by relatively soft X-ray fluxes below 2.5 keV. In the hard

---

band ($E > 2.5$ keV), the measured X-ray flux is probably poorly constrained, except for the brightest sources. As a consequence, the scatter of the hard X-ray luminosities is large and no definitive fit possible.
2. S06, based on uniform X-ray data and homogeneous observations, state that the observed dependence between intrinsic L_X and L_{bol} is much tighter than was thought before, with the residual dispersion of the $L_X - L_{bol}$ relation around the least-square scaling law being less or equal to some 20%, if one excludes binary stars and stars later than O9. Our current results are unable to confirm this statement due to a larger scatter in the data owing to the patchy ISM absorption in the Carina region.
3. *On average*, the *observed* X-ray properties of O binary stars are not very different from those of single stars (cf. our Figs. 14 and 16 from S06). We shall discuss possible reasons for this behaviour below.

7.3. On the origin of the $L_X - L_{bol}$ scaling for single stars

It has been pointed out many times in the literature that the scaling relation between L_X and L_{bol} could be an indirect effect. Indeed, the common paradigm for the generation of X-rays in early-type stars is a wind shock model (see e.g. Lucy & Solomon 1970; Owocki & Cohen 1999; Dessart & Owocki 2005). If X-ray emission is formed throughout the wind then L_X should be proportional to some combination of wind parameters like the mass loss rate $\dot{M}$ and the terminal wind velocity v_∞. Indeed, Owocki & Cohen (1999) from the exospheric approximation established that the X-ray luminosity should scale with the mean wind density $\dot{M}/v_\infty$ in the form $L_X \sim (\dot{M}/v_\infty)^2$ for optically thin winds and $L_X \sim (\dot{M}/v_\infty)^{(1+s)}$ for optically thick winds, with s being the index of the radial power law dependence of the X-ray filling factor $f \sim r^s$. However, Sana et al. (2006) state that these considerations contrast with the observed tight dependence between L_X and L_{bol}.

A new idea about the origin of X-rays from single O-type stars was recently brought forward by Pollock (2007). It is based on the fact that, according to recent *XMM-Newton* high resolution observations of ζ Orionis, all emission lines have the same velocity profile which contrast with the paradigm of wind shocks, in which line profiles should be dependent on the global kinematic structure of the wind. The principal difference between the two models is that in the traditional wind shock model the energy exchange between post-shock ions and electrons occurs on a short time scale while Pollock estimates the ion-ion collisional mean-free path and find that at least in the case of ζ Orionis it can be quite large, which leads to very slow energy exchange between hot ions and cold electrons. He further suggest that the shocks are collisionless and that the ionization of the post-shock gas is not caused by electrons as in the traditional picture but rather by protons. The line profiles then are defined not by macroscopic motion of ionized gas but simply by the line-of-sight component of the thermalized motion of ions in the immediate post-shock gas. This idea has not yet been developed up to a stage when numerical modeling could be done and a theoretical connection between L_X and L_{bol} (if any) established.

From the observational point of view, we agree with S06 that whatever the theoretical explanation behind the $L_X - L_{bol}$ relation, it is a firmly established observational fact which should be explained by a future theory. Not only is the proportionality itself now well established but also some of its more detailed characteristics (see items $1-3$ above).

---

[3] The X-ray bands of S06 are almost identical to ours.

7.4. Binary versus single stars

Item (3) in the above list requires special consideration. It was already mentioned in the introduction that, in a binary system consisting of two early-type stars, the supersonic winds of the components will inevitably collide. The key feature of the wind-wind collision, making it different from localized shocks formed by internal line-driven instability of supersonic winds is that the relative velocity of the two flows is very high, of the order of thousands km s^{-1}, at least along the line connecting the centers of the components. For comparison, the velocity differences in localized shocks within a wind are typically of the order of a few hundred km s^{-1}. As a result, X-ray emission from binary early-type stars should be more luminous and *harder* than in single stars. This was understood long ago (Prilutskii & Usov 1976; Cherepashchuk 1976). One of the first theoretical predictions about the hardness and X-ray luminosity of binary early-type stars was made by Usov (1992) and later on was refined and quantified in numerical gas-dynamical simulations (see, e.g. Stevens & Pittard 1999).

Over the years, it became clear that the original somewhat *naive* expectations of more luminous and hard X-ray radiation from colliding wind binaries had to be significantly adjusted. A large number of factors play a role in the X-ray output of a binary, such as the orbital period (hence the distance between the components, the pre-shock velocity and the density in the collision zone), the wind momentum ratio, the orbital inclination, the eccentricity, etc. These factors influence both the rate of intrinsic X-ray production in the collision zone and the absorption of the X-rays within the winds of the components. For additional discussion, see a recent paper by Linder et al. (2006).

It is nevertheless still puzzling that so few early-type binaries are significantly more luminous and harder than the total sample of O-type stars (e.g. in our Figs. 14 and in 16 of S06, also see Raassen et al., 2003 who present a collection of X-ray properties of single and binary early-type stars). Two intriguing questions already mentioned in the introduction are (i) why some known colliding wind binaries have soft X-ray spectra and (ii) why some stars having hard X-ray spectra (as demonstrated e.g. by the presence of the Fe XXV−XXVI lines at ~6.7 keV) lack any evidence of binarity?

The answer to the first question may be two-fold. First, it may be partly the problem of the detection of the hard X-ray spectral tail in relatively faint colliding wind binaries. On the other hand, theoretical studies of wind-wind collision mechanisms (Stevens & Pollock 1994; Owocki & Gayley 1995; Walder & Folini 2003; Antokhin et al. 2004) suggest that either the so-called radiative braking or radiative inhibition (mutual radiative influence of the binary components on the wind of their vis-à-vis) may significantly slow down the winds of the binary components just before the collision, thus reducing the X-ray luminosity of the system and the hardness of its X-ray spectrum (which is proportional to the square of the wind velocity entering the collision zone). To verify this possibility, we shall apply the recent models accounting for this phenomenon, in our forthcoming analysis of the binary HD 93205 which has one of the best X-ray coverages of the orbital cycle of any early-type binary.

There is probably no single answer to the second question, either. In some cases (most notably WR 25 and MJ 596) it was recently found (see references above) that these hard X-ray sources are indeed binary systems that escaped detection before. These recent advances raise interest in a similar case of a bright O3 V star HD 93250 (showing clear indication of the Fe XXV-XXVI lines). The star does not display any radial velocity or photometric variability and as such was considered as single. However, it was reported to display non-thermal radio emission (Leitherer et al. 1995) and this feature is nowadays often believed to be evidence for a colliding wind system also in O+O binaries. On the other hand, the O8.5 V star CPD −59°2629 which is also an unusually bright and hard X-ray source for its spectral type might be an example of a star with a magnetically confined wind (ud-Doula et al. 2006). A low-mass companion with high activity could also be considered.

8. Conclusions

High quality and large amounts of *XMM-Newton* data obtained for the Carina Nebula, allowed us to detect 235 discrete sources in the field of view. Several of these sources are probably pre-main sequence stars with a characteristic short-term variability, while seven sources are recognized as possible background AGNs.

We concentrated in our study on the properties of early-type stars in the region. Spectral analyses of twenty four sources of type OB and WR 25 were performed. We derived the spectral parameters of the sources and their fluxes in three energy bands. Estimating a value of interstellar absorption towards every source and assuming a distance of 2.5 kpc to the Nebula, we derived the X-ray luminosities of these stars. Comparison of these luminosities with bolometric luminosities has confirmed the known scaling relation $L_X \sim 10^{-7} \times L_{\rm bol}$ for early type stars and allowed us to make a few more detailed statements about the characteristics of this relation. We pointed out that, *on average*, the observed X-ray properties of binary and single early type stars are similar, and give several possible explanations for this fact.

Further work will be aimed at the detailed analysis of the data of particular sources.

References

Albacete-Colombo, J. F., Méndez, M., & Morrell, N. I. 2003, MNRAS, 346, 704
Allen, D. A., & Hillier, D. J. 1993, Proc. Astron. Soc. Australia, 10, 338
Antokhin, I. I., Owocki, S. P., & Brown, J. C. 2004, ApJ, 611, 434
Antokhina, E. A., Moffat, A. F. J., Antokhin, I. I., Bertrand, J.-F., & Lamontagne, R. 2000, ApJ, 529, 463
Bauer, F. E., Vignali, C., Alexander, W. N., et al. 2004, Adv. Space Res., 34, 2555
Berghöfer, T. W., Schmitt, J. H. M. M., & Cassinelli, J. P. 1997, A&AS, 118, 481 (erratum, A&AS, 121, 212)
Bessell, M. S., & Brett, J. M. 1988, PASP, 100, 1134
Bohlin, R. C., Savage, B. D., & Drake, J. F. 1978, ApJ, 224, 132
Briggs, K. R., & Pye, J. P. 2003, MNRAS, 345, 714
Brown, J. C., Telfer, D. C., Hanuschik, R. W., & Cassinelli, J. P. 2003, in Magnetic Fields in O, B and A Stars: Origin and Connection to Pulsation, Rotation and Mass Loss, ed. L. A. Balona, H. F. Henrichs, & R. Medupe (San Francisco: ASP), ASP Conf. Ser., 305, 285

Carpenter, J. M. 2001, AJ, 121, 2851

Carraro, G., Romaniello, M., Ventura, P., & Patat, F. 2004, A&AS, 418, 525

Cassinelli, J. P., Brown J. C., Maheswaran, M., Miller, N. A., & Telfer, D. 2002, ApJ, 578, 951

Cherepashchuk, A. M. 1976, Sov. Astron. Lett., 2, 138

Chlebowski, T., Harnden, F. R., Jr., & Sciortino, S. 1989, ApJ, 341, 427

Corcoran, M. F. 1999, Rev. Mex. Astron. Astrofis. Ser. Conf., 8, 131

Corcoran, M. F. 2005, AJ, 129, 2018

Corcoran, M. F., Fredericks, A. C., Petre, R., Swank, J. H., & Drake, S. A. 2000, ApJ, 545, 420

Cudworth, K. M., Martin, S. C., & DeGioia-Eastwood, K. 1993, AJ, 105, 1822

Davidson, K., Smith, N., Gull, Th. R., Ishibashi, K., & Hillier, D. J. 2001, AJ, 121, 1569

DeGioia-Eastwood, K., Throop, H., Walker, G., & Cudworth, K. M. 2001, ApJ, 549, 578

Dessart, L., & Owocki, S. P. 2002, A&A, 383, 1113

Dessart, L., & Owocki, S. P. 2005, A&A, 437, 657

Evans, N. R., Seward, F. D., Krauss, M. I., et al. 2003, ApJ, 589, 509

Evans, N. R., Schlegel, E. M., Waldron, W. L., et al. 2004, ApJ, 612, 1065

Favata, F. 2005, Mem. S. A. It., 76, 337

Favata, F., Flaccomio, E., Reale, F., et al. 2005, ApJS, 160, 469

Feinstein, A., Marraco, H. G., & Muzzio, J. 1973, A&AS, 12, 331

Feldmeier, A., Kudritzki, R.-P., Palsa, R., Pauldrach, A. W. A., & Puls, J. 1997, A&A, 320, 899

Fiore, F. 1997, Mem. S. A.It., 68, 119

Freyhammer, L. M., Clausen, J. V., Arentoft, J., & Sterken, C. 2001, A&A, 369, 561

Gagné, M., Oksala, M. E., Cohen, D. H., et al. 2005, ApJ, 628, 986

Giacconi, R., Rosati, P., Tozzi, P., et al. 2001, ApJ, 551, 624

Giardino, G., Favata, F., Micela, G., & Reale, F. 2004, A&AS, 413, 669

Hamaguchi, K., Corcoran, M. F., Gull, T., et al. 2007, ApJ, 663, 552

Jeffries, R. D., Thurston, M. R., & Pye, J. P. 1997, MNRAS, 287, 350

Kahn, S. M., Leutenegger, M. A., Cottam, J., et al. 2001, A&A, 365, L312

Kudritzki, R. P., Palsa, R., Feldmeier, A., Puls, J., & Pauldrach, A. W. A. 1996, in Röntgenstrahlung from the Universe, ed. H. U. Zimmermann, J. Trümper, & H. York, 9

Lada, C. J., & Adams, F. C. 1992, ApJ, 393, 278

Leitherer, C., Chapman, J. M., & Koribalski, B. 1995, ApJ, 450, 289

Leutenegger, M. A., Kahn, S. M., & Ramsay, G. 2003, ApJ, 585, 1015

Levato, H., Malaroda, S., Morrell, N., Garcia, B., & Hernández, C. 1991, ApJS, 75, 869

Li, Q., Cassinelli, J. P., Brown, J. C., Waldron, W., & Miller, N. A. 2007, ApJ, in press

Linder, N., Rauw, G., Pollock, A. M. T., & Stevens, I. R. 2006, MNRAS, 370, 1623

Long, K. S., & White, R. L. 1980, ApJ, 239, L65

Lucy, L. B. 1982, ApJ, 255, 286

Lucy, L. B., & Solomon, P. M. 1970, ApJ, 159, 879

Lucy, L. B., & White, R. L. 1980, ApJ, 241, 300

Maheswaran, M. 2003, ApJ, 592, 1156

Massey, P., & Johnson, J. 1993, AJ, 105, 980

Massey, P., Waterhouse, E., & DeGioia-Eastwood, K. 2000, AJ, 119, 2214

Massey, P., DeGioia-Eastwood, K., & Waterhouse, E. 2001, AJ, 121, 1050

Meaburn, J. 1999, in Eta Carinae at the Millenium, ed. J. A. Morse, R. M. Humphreys, & A. Damineli (San Francisco: ASP), ASP Conf. Ser., 179, 89

Megeath, S. T., Cox, P., Bronfman, L., & Roelfsema, P. R. 1996, A&A, 305, 296

Meyer, M. R., Calvet, N., & Hillenbrand, L. A. 1997, AJ, 114, 288

Morrell, N. I., Barbá, R. H., Niemela, V. S., et al. 2001, MNRAS, 326, 85

Motch, C., Herent, O., & Guillout, P. 2003, Astron. Nachr., 324, 61

Nandra, K. 2001, Adv. Space Res., 28, 295

Nazé, Y., Antokhin, I. I., Sana, H., Gosset, E., & Rauw, G. 2005, MNRAS, 359, 688

Niemela, V. S., Morrell, N. I., Fernández Lajús, E., et al. 2006, MNRAS, 367, 1450

Owocki, S. P., & Cohen, D. H. 1999, ApJ, 520, 833

Owocki, S. P., & Gayley, K. G. 1995, ApJ, 454, L145

Pallavicini, R., Golub, L., Rosner, R., et al. 1981, ApJ, 248, 279

Pollock, A. M. T. 1995, in Wolf-Rayet Stars: Binaries, Colliding Winds, Evolution, ed. K. A. van der Hucht, & P. M. Williams (Dordrecht: Kluwer), Proc. IAU Symp., 163, 429

Pollock, A. M. T. 2007, A&A, 463, 1111

Pollock, A. M. T., & Corcoran, M. F. 2006, A&A, 445, 1093

Preibisch, T., & Zinnecker, H. 2002, AJ, 123, 1613

Press, W. H., Teukolsky, S. A., Vetterling, W. T., et al. 1992, Numerical recipes in C, second edition (Cambridge University Press), Chap. 15.2, 664

Prilutskii, O. F., & Usov, V. V. 1976, SvA, 20, 2

Raassen, A. J. J., van der Hucht, K. A., Mewe, R., et al. 2003, A&A, 402, 653

Rathborne, J. M., Burton, M. G., Brooks, K. J., et al. 2002, MNRAS, 331, 85

Rauw, G. 2004, in Evolution of Massive Stars, Mass Loss and Winds, ed. M. Heydari-Malayeri, P. Stee, & J.-P. Zahn, EAS Publ. Ser., 13, 293

Rauw, G. 2006, in The X-ray Universe 2005, ESA, SP-604, 7

Rauw, G., Sana, H., Antokhin, I. I., et al. 2001, MNRAS, 326, 1149

Rauw, G., Nazé, Y., Gosset, E., et al. 2002, A&A, 395, 499

Rauw, G., De Becker, M., Gosset, E., Pittard, J. M., & Stevens, I. R. 2003, A&A, 407, 925

Raymond, J. C., & Smith, B. W. 1977, ApJS, 35, 419

Sana, H., Stevens, I. R., Gosset, E., Rauw, G., & Vreux, J.-M. 2004, MNRAS, 350, 809

Sana, H., Rauw, G., Nazé, Y., Gosset, E., & Vreux, J.-M. 2006, MNRAS, 372, 661

Sana, H., Rauw, G., Sung, H., Gosset, E., & Vreux, J.-M. 2007, MNRAS, 377, 945

Sanchawala, K., Chen, W.-P., Lee, H.-T., et al. 2007, ApJ, 656, 452

Schlegel, D. J., Finkbeiner, D. P., & Davis, M. 1998, ApJ, 500, 525

Serio, S., Reale, F., Jakimiec, J., Sylwester, B., & Sylwester, J. 1991, A&AS, 241, 197

Seward, F. D., & Chlebowski, T. 1982, ApJ, 256, 530

Seward, F. D., Forman, W. R., Giacconi, R., et al. 1979, ApJ, 234, L55

Skinner, S. L., Nagase, F., Koyama, K., Maeda, Y., & Tsuboi, Y. 1995, in Wolf-Rayet Stars: Binaries, Colliding Winds, Evolution, ed. K. A. van der Hucht, & P. M. Williams (Dordrecht: Kluwer), Proc. IAU Symp., 163, 471

Skinner, S. L., Zhekov, S. A., Güdel, M., & Schmutz, W. 2002, ApJ, 572, 477

Skrutskie, M. F., Schneider, S. E., Stiening, R., et al. 1997, in The Impact of Large Scale Near-IR Sky Surveys, ed. F. Garzon et al. (Dordrecht: Kluwer Acad. Pub.), 25

Smith, R. K., Brickhouse, N. S., Liedahl, D. A., & Raymond, J. C. 2001, ApJ, 556, L91

Smith, N., Bally, J., & Morse, J. A. 2003, ApJ, 587, L105

Stephenson, C. B., & Sanduleak, N. 1971, Publication of the Warner and Swasey Observatory, Cleveland, Ohio: Case Western Reserve University, 1, 1

Stevens, I. R., & Pittard, J. M. 1999, in Wolf-Rayet Phenomena in Massive Stars and Starburst Galaxies, ed. K. A. van der Hucht et al. (San Francisco: ASP), Proc. IAU Symp., 193, 289

Stevens, I. R., & Pollock, A. M. T. 1994, MNRAS, 269, 226

Stevens, I. R., Blondin, J. M., & Pollock, A. M. T. 1992, ApJ, 386, 265

Tapia, M., Roth, M., Vázquez, R. A., & Feinstein, A. 2003, MNRAS, 339, 44

ud-Doula, A., Townsend, R. H. D., & Owocki, S. P. 2006, ApJ, 640, 191

Usov, V. V. 1992, ApJ, 389, 635

Viotti, R. F., Antonelli, L. A., Rossi, C., & Rebecchi, S. 2004, A&A, 420, 527

Walborn, N. R. 1995, Rev. Mex. Astron. Astrofis. Ser. Conf., 2, 51

Walder, R., & Folini, D. 2003, in A Massive Star Odyssey: From Main Sequence to Supernova, ed. K. A. van der Hucht, A. Herrero, & E. César (San Francisco: ASP), Proc. IAU Symp., 212, 139

Waldron, W. L. 1984, ApJ, 282, 256

Weis, K., Corcoran, M. F., Bomans, D. J., & Davidson, K. 2004, A&A, 415, 595

Online Material

Table 2. Sample of the X-ray catalogue.

X# [1]	Var Status [2]	Data Set [3]	L_2^{PN} [4]	cr_{PN} [5]	σ_{PN} [6]	$cr_{\mathrm{PN}}^{\mathrm{S}}$ [7]	$\sigma_{\mathrm{PN}}^{\mathrm{S}}$ [8]	$cr_{\mathrm{PN}}^{\mathrm{M}}$ [9]	$\sigma_{\mathrm{PN}}^{\mathrm{M}}$ [10]	$cr_{\mathrm{PN}}^{\mathrm{H}}$ [11]	$\sigma_{\mathrm{PN}}^{\mathrm{H}}$ [12]
1	Uncert	3	37.0	11.6964	1.8388	7.5714	1.5446	4.1250	0.9757	0.0000	0.2079
		5	67.8	14.3821	1.6988	9.8716	1.4067	3.6847	0.7888	0.8258	0.5338
2	Const	3	78.9	11.0794	1.5107	1.0840	0.7725	4.9085	0.8522	5.0868	0.9793
		5	155.1	13.0312	1.2820	0.0000	0.3180	5.0587	0.7272	7.9724	1.0067
3	Noinfo	3	5.9	1.5988	0.6920	0.0000	0.3058	0.0631	0.2185	1.5357	0.5810
4	Var	3	14.2	13.1136	3.7333	3.0763	2.6452	6.8288	2.0792	3.2085	1.6178
		4	257.1	30.2308	2.6712	6.3221	1.5744	19.5985	1.8292	4.3102	1.1448
		5	165.1	18.3160	1.7907	5.1892	1.2056	10.6765	1.1067	2.4504	0.7269
5	Uncert	3	27.6	6.2785	1.2448	4.3118	0.9343	1.2414	0.5292	0.7254	0.6297
		4	46.6	8.9067	1.4053	5.4440	1.0365	2.8946	0.7262	0.5681	0.6108
		5	25.8	4.7296	0.9220	3.1683	0.7315	1.3936	0.4500	0.1676	0.3355
6	Const	3	41.6	8.5184	1.6391	0.7818	0.9702	2.2362	0.7546	5.5004	1.0844
		5	59.4	8.3989	1.3907	0.0000	0.7206	2.0239	0.6175	6.3750	1.0165
7	Const	3	27.9	6.7066	1.7137	0.9344	1.1214	5.7722	1.1112	0.0000	0.6666
		4	3.0	2.7511	1.4317	0.7435	0.9801	2.0076	0.8730	0.0000	0.5718
8	Const	3	64.3	11.2433	1.4168	7.0934	1.1558	4.1499	0.7856	0.0000	0.2330
		4	81.9	11.4430	1.3621	6.0041	1.0333	5.4389	0.8331	0.0000	0.3058
		5	89.4	11.0901	1.2253	7.4002	1.0139	3.6899	0.6185	0.0000	0.3015

X# [1]	Var Status [2]	Data Set [3]	L_2^{MOS1} [13]	cr_{MOS1} [14]	σ_{MOS1} [15]	$cr_{\mathrm{MOS1}}^{\mathrm{S}}$ [16]	$\sigma_{\mathrm{MOS1}}^{\mathrm{S}}$ [17]	$cr_{\mathrm{MOS1}}^{\mathrm{M}}$ [18]	$\sigma_{\mathrm{MOS1}}^{\mathrm{M}}$ [19]	$cr_{\mathrm{MOS1}}^{\mathrm{H}}$ [20]	$\sigma_{\mathrm{MOS1}}^{\mathrm{H}}$ [21]
1	Uncert	3	2.8	1.5736	0.7445	0.2249	0.3832	1.1755	0.5769	0.1732	0.2732
		5	30.0	4.5064	0.8380	2.3016	0.6342	2.2048	0.5365	0.0000	0.1103
2	Const	3	41.7	3.7951	0.7415	0.0000	0.1756	2.1814	0.5132	1.6137	0.5057
		5	54.6	4.0763	0.6695	0.1027	0.2009	1.7207	0.3944	2.2529	0.5023
3	Noinfo	3	6.3	1.1639	0.4805	0.0000	0.1250	0.4476	0.3061	0.7163	0.3486
4	Var	3	26.8	5.4286	1.0912	1.3413	0.6648	3.0680	0.7086	1.0192	0.4967
		4	116.8	11.9558	1.3586	2.6415	0.7379	6.3675	0.8938	2.9468	0.7088
		5	66.2	7.3132	1.0267	1.9323	0.6414	3.8654	0.6433	1.5155	0.4785
5	Uncert	3	10.7	1.8870	0.6134	0.7426	0.3567	0.8337	0.3534	0.3107	0.3524
		4	25.3	3.5911	0.8622	1.1051	0.4992	2.4859	0.6274	0.0000	0.3171
		5	6.5	1.2127	0.4765	1.0220	0.4014	0.1907	0.2387	0.0000	0.0948
6	Const	3	8.0	1.8536	0.7433	0.0000	0.3138	0.2292	0.3111	1.6244	0.5977
		5	15.4	2.5796	0.7105	0.1040	0.2827	0.8577	0.4188	1.6178	0.4994
7	Const	3	3.8	1.6451	0.7503	0.2117	0.4138	0.9603	0.4802	0.4731	0.4013
		4	1.5	0.9795	0.6168	0.0000	0.2356	0.6828	0.4627	0.2968	0.3328
8	Const	3	26.0	3.5804	0.7153	1.7610	0.5240	1.7545	0.4686	0.0648	0.1322
		4	39.5	4.2651	0.7098	2.9362	0.5725	1.0653	0.3545	0.2635	0.2246
		5	27.0	3.1810	0.5963	1.9396	0.4694	1.2414	0.3615	0.0000	0.0678

X# [1]	Var Status [2]	Data Set [3]	L_2^{MOS2} [22]	cr_{MOS2} [23]	σ_{MOS2} [24]	$cr_{\mathrm{MOS2}}^{\mathrm{S}}$ [25]	$\sigma_{\mathrm{MOS2}}^{\mathrm{S}}$ [26]	$cr_{\mathrm{MOS2}}^{\mathrm{M}}$ [27]	$\sigma_{\mathrm{MOS2}}^{\mathrm{M}}$ [28]	$cr_{\mathrm{MOS2}}^{\mathrm{H}}$ [29]	$\sigma_{\mathrm{MOS2}}^{\mathrm{H}}$ [30]
1	Uncert	3	16.9	3.7830	0.9184	2.4310	0.7169	1.3520	0.5082	0.0000	0.2671
		5	21.8	3.3101	0.7358	1.2515	0.5254	1.9346	0.4799	0.1240	0.1872
2	Const	3	16.9	3.7571	1.0486	0.0000	0.2600	1.8097	0.6987	1.9474	0.7375
		5	19.2	3.6836	0.9986	0.0000	0.1867	0.8314	0.5721	2.8522	0.7969
3	Noinfo	3	5.3	1.2067	0.5056	0.0287	0.1578	0.3144	0.2606	0.8636	0.4035
4	Var	3	35.8	5.1319	0.9696	1.5404	0.6497	2.7681	0.6045	0.8234	0.3904
		4	75.6	7.5895	1.0367	1.4724	0.5831	4.3611	0.7020	1.7560	0.4919
		5	45.2	4.1332	0.7263	0.2420	0.3470	2.9420	0.5314	0.9493	0.3531
5	Uncert	3	1.9	0.6367	0.5123	0.6367	0.3823	0.0000	0.1562	0.0000	0.3032
		4	34.9	3.3469	0.6648	1.6299	0.4648	1.6700	0.4481	0.0470	0.1584
		5	14.5	1.7518	0.4607	1.0534	0.3500	0.6985	0.2908	0.0000	0.0721
6	Const	3	7.7	1.3382	0.6299	0.0000	0.3383	0.0900	0.2523	1.2483	0.4676
		5	15.7	1.9042	0.5742	0.0000	0.2060	0.4021	0.3204	1.5021	0.4297
7	Const	3	3.6	1.7374	0.7574	0.6287	0.5433	0.9286	0.4724	0.1802	0.2353
		4	1.7	0.6576	0.5783	0.0000	0.3803	0.6576	0.3924	0.0000	0.1893
8	Const	3	22.2	3.4013	0.7177	2.2301	0.5873	1.1712	0.4071	0.0000	0.0666
		4	22.4	2.9989	0.6168	1.7462	0.4723	1.2527	0.3939	0.0000	0.0468
		5	18.6	2.6419	0.5682	1.4887	0.4440	1.1532	0.3414	0.0000	0.0958

The first column gives the source number. The second column provides the set-to-set variability status of the source (see Sect. 5.2). The third column gives the data set number in which the count rates of the source were measured. Columns 4−12 (resp. 13−21 and 22−30) give the logarithmic likelihood L_2 for the given instrument, the total count rate cr in the whole energy band (0.4−10.0 keV) and its associated error (σ), the count rates in the three different energy bands (S: [0.4−1.0 keV], M: [1.0−2.5 keV], H: [2.5−10.0 keV]) and their errors. The count rates and the related uncertainties are all expressed in 10^{-3} counts s^{-1}.

Table 3. Sample of the cross identification table of X-ray sources detected in our EPIC images of the Carina Nebula.

X#	XMMU J	RA	Dec	AC03	EV03	Nr.	d (")	J	H	K_S	V	B − V	U − B	Optical Name	Spectral type	Ref.	Member (%)
[1]	[2]	[3]	[4]	[5]	[6]	[7]	[8]	[9]	[10]	[11]	[12]	[13]	[14]	[15]	[16]	[17]	[18]
1	104236.8−594357	10 42 36.83	−59 43 57.9	−	−	0	3.9	13.00	12.37	12.18							
2	104256.6−594220	10 42 56.61	−59 42 20.2	−	−	2											
3	104303.2−593949	10 43 03.21	−59 39 49.3	−	−	0											
4	104304.4−594902	10 43 04.43	−59 49 02.7	−	−	1	3.9	16.15	14.41	14.20	12.47	0.38	−0.80	MJ 3		MJ	
5	104307.8−593557	10 43 07.82	−59 35 57.4	−	−	1	3.7	13.76	13.05	12.83							
6	104310.5−595012	10 43 10.56	−59 50 12.6	−	−	0											
7	104310.9−595124	10 43 10.91	−59 51 24.7	−	−	1	1.4	13.75	12.97	12.57							
8	104311.4−594423	10 43 11.40	−59 44 24.0	−	−	1	3.3	8.70	8.62	8.50	9.64	0.26	−0.76	HDE 303316		MJ	
9	104315.1−593344	10 43 15.12	−59 33 44.2	−	−	1	3.1	12.77	12.30	12.14							
10	104317.5−593321	10 43 17.55	−59 33 21.7	−	−	0											
11	104319.8−594248	10 43 19.86	−59 42 48.5	−	−	1	2.9	15.15	14.15	13.58							
12	104320.6−594619	10 43 20.63	−59 46 19.8	−	−	1	2.5	14.45	13.52	13.21							
13	104325.9−594720	10 43 25.93	−59 47 20.5	−	−	0											
14	104326.8−595251	10 43 26.90	−59 52 51.5	−	−	0											
15	104327.4−594202	10 43 27.48	−59 42 02.4	−	−	0											
16	104329.8−593344	10 43 30.03	−59 33 48.0	1	−	1	3.0	13.41	12.52	12.21							
17	104333.7−594030	10 43 33.76	−59 40 30.0	−	−	1	2.3	15.49	14.69	14.49							
18	104339.9−593445	10 43 39.92	−59 34 50.9	−	−	1	2.3	13.21	12.26	11.96	15.43	1.35		DETWC-14 18		DETWC	
19	104340.7−594638	10 43 40.75	−59 46 38.4	−	−	0											
20	104341.2−593355	10 43 41.23	−59 33 55.7	−	−	1	3.3	11.23	10.80	10.55	17.82	0.75	0.69	DETWC-14 29		DETWC	
21	104341.3−593205	10 43 41.49	−59 32 09.8	3	−	1	3.5	12.70	11.97	11.71	15.72	1.30		DETWC-14 43		DETWC	
22	104341.4−594223	10 43 41.61	−59 42 26.8	4	−	2											
23	104343.0−594411	10 43 43.04	−59 44 11.3	−	−	1	3.4	15.63	14.31	13.27							
24	104343.1−593555	10 43 43.16	−59 35 55.7	−	−	1	3.9	14.41	13.49	13.12							
25	104344.6−593459	10 43 44.64	−59 34 59.1	−	−	2								DETWC-14 76, 65		MJ	
26	104345.0−595327	10 43 45.08	−59 53 27.7	8	−	1	2.3	10.02	9.99	9.97	10.43	0.14	−0.77	MJ 126		MJ	
27	104345.4−594159	10 43 45.43	−59 41 59.8	−	−	1	3.3	14.37	12.99	12.18							
28	104345.6−593431	10 43 45.60	−59 34 31.6	−	−	1	2.7	13.24	12.42	12.17				DETWC-14 78, 81			
29	104346.0−593221	10 43 46.05	−59 32 21.6	−	−	1	0.1	15.26	14.12	13.51							
30	104346.3−593256	10 43 46.36	−59 32 56.6	−	−	1	3.2	8.66	8.52	8.50	9.65	0.20	−0.63	CPD−58° 2611 = Tr 14 20	O6 V(f)	MJ	96
31	104346.3−593116	10 43 46.39	−59 31 16.5	−	−	1	2.6	12.37	11.70	11.51							
32	104347.3−593244	10 43 47.35	−59 32 44.2	−	−	1	3.0	12.05	11.56	11.30	15.20	1.36	0.77	DETWC-14 107		DETWC	
33	104348.8−593324	10 43 48.88	−59 33 24.6	−	−	1	1.4	9.55	9.39	9.26	10.73	0.35	−0.55	Tr 14 21	O9 V	MJ	81
34	104349.2−593404	10 43 49.22	−59 34 05.0	−	−	1	2.0	14.30	13.13	12.54							
35	104349.8−594453	10 43 49.45	−59 44 56.9	8	−	1	2.0	12.67	12.20	12.06	14.34	0.77	−0.09	Tr 14 Y 334		Cud	0
36	104351.0−595239	10 43 51.03	−59 52 40.0	−	−	1	2.9	12.00	11.60	11.50	13.75	0.41		MJ 156		MJ	
37	104351.4−593117	10 43 51.47	−59 31 17.1	−	−	1	2.4	13.56	12.89	12.63							
38	104351.6−593244	10 43 51.63	−59 32 44.3	−	−	1	3.1	13.00	12.27	11.94	16.38	1.26		DETWC-14 160		DETWC	
39	104352.1−593556	10 43 52.02	−59 35 58.0	9	−	1	1.9	13.28	12.55	12.22	16.58	1.44		DETWC-14 167		DETWC	
40	104352.3−593924	10 43 52.48	−59 39 24.7	10	−	1	2.8	13.03	11.91	11.20							
41	104355.0−593130	10 43 55.09	−59 31 30.0	−	−	1	1.7	13.26	12.51	12.26	16.53	1.46		DETWC-14 200		DETWC	
42	104355.2−593200	10 43 55.23	−59 32 00.7	−	−	2	2.4	10.51	10.04	9.70	12.52	0.78	0.43	Tr 14 14		DETWC	78
43	104355.9−594926	10 43 55.92	−59 49 26.1	−	−	0											
44	104356.0−593515	10 43 56.03	−59 35 15.1	−	−	0											
45	104356.7−593252	10 43 57.39	−59 32 54.8	11c	103	2								HD 93129 A + B			

The first and second columns yield the number of the X-ray source as well as the name according to the naming conventions for serendipitous *XMM-Newton* sources. To avoid duplicating the nomenclature, AC03 names are given for the sources cross-identified with the AC03 catalogue. The third and fourth columns provide the *XMM-Newton* coordinates of the sources. Columns [5] and [6] list the star number in the X-ray catalogues of AC03 and EV03 according to our identification. Columns [7] to [11] summarize the results of the cross-correlation with the 2MASS catalogue. The columns labelled "Nr." and "*d*" yield the number of 2MASS counterparts within a 4.0″ radius and the angular separation between the X-ray source and the IR counterpart. Columns [12] to [17] provide information on the properties of optical counterparts (when available). DETWC-14 and DETWC-16 names yield the sequence number of the optical star in the catalogue of DeGioia-Eastwood et al. (2001) for the Tr 14 and Tr 16 clusters respectively. In a similar way, Tr 14 and Tr 16 numbers refer to the numbering scheme introduced by Feinstein et al. (1973) whilst Tr 14 Y and Tr 16 Y correspond to the convention of Cudworth et al. (1993). Finally, MJ numbers are taken from Massey & Johnson (1993). The column labelled "Ref." yields the reference for the optical photometry whilst the last column indicates the membership probability from the proper motion study of Cudworth et al. (1993).